# 5th European Conference on Plasma Diagnostics

April 23 - 27 **2023**

**Rethymno, Crete, Greece**

https://ecpd2023.eventsadmin.com

**COST Action 21128**
**PROBONO Meeting**

April 28 **2023**

**electronic proceedings volume**

**Topics:**

- Magnetic Confinement Fusion (MCF)
- Beam Plasmas and Inertial Fusion (BPIF)
- Low-Temperature and Industrial Plasmas (LTIP)
- Basic and Astrophysical Plasmas (BAP)

# Oral presentations:

**Oral 4** Carlos Salgado

**Angular-resolved thomson parabola spectrometer for Laser-plasma ion accelerators**

**Oral 15** Giorgio Finocchiaro

**Space resolved Electron density and temperature evaluation by XRay pinhole camera in ECR Plasma**

**Oral 19** Oldrich Renner

**1d space-time & 2d space resolved hot electron generation at shock ignition relevant parameters**

**Oral 24** Emanouil Benis

**Coherent xuv multispectral diffraction imaging in Reflection mode and prospect in dense plasma diagnostics**

**Oral 35** Diogo R. Ferreira

**Improving the time resolution of thomson scattering via machine learning on reflectometry data**

**Oral 39** Filipe da Silva

**Status of the EUROfusion Enabling Research Project: Advances in real-time reflectometry plasma tracking, for next generation machines**

# Poster Presentations

**P1-8** Andrea Belpane
Conceptual design of a visible spectroscopy diagnostic for DTT

**P2- 6** Hisamichi Funaba
Real-time electron temperature and density measurement by thomson scattering for plasma control on LHD

**P2-16** Francesca Bombarda
CVD Diamond tomography for the DTT fusion device

**P2-22** Umar Sheikh
CCD direct detection on a SPRED spectrometer

**P3-20** Christopher Muscatello
Status of the Development and Testing of Port-Plug and ECH-Protection Components for the ITER Low-Field Side Reflectometer

# ANGULAR-RESOLVED THOMSON PARABOLA SPECTROMETER FOR LASER-PLASMA ION ACCELERATORS

C. Salgado-López[1], J.I. Apiñaniz[1], A. Curcio[2], D. de Luis[1], J. L. Henares[1], J. A. Pérez-Hernández[1], L. Volpe[1,3] and G. Gatti[1]

[1]Centro de Láseres Pulsados (CLPU), Salamanca, Spain.
[2]Laboratori Nazionali di Frascati (INFN-LNF), Frascati, Italy.
[3]Universidad Politécnica de Madrid (UPM), Madrid, Spain.
csalgado@clpu.es

**Abstract**

Laser-plasma driven accelerators have become reliable sources of low-emittance, broadband and multi-species ion beams, presenting cut-off energies above the MeV-level. We report on the development, construction, and experimental test of an angle-resolved Thomson Parabola (TP) spectrometer for laser-accelerated multi-MeV ion beams which is able to distinguish between ionic species with different $q/m$ ratio. The angular resolving power is achieved due to an array of entrance pinholes and it can be simply adjusted by modifying the geometry of the experiment and/or the pinhole array itself. The analysis procedure allows different ion traces to cross on the detector plane, which greatly enhances the flexibility and capabilities of the detector. A full characterization of the TP magnetic field has been implemented into a relativistic code developed for the trajectory calculation of each beamlet. High repetition rate compatibility is guaranteed by the use of a microchannel plate (MCP). We describe the first test of the spectrometer at the 1 PW VEGA 3 laser facility at CLPU, Salamanca (Spain), where up to 15 MeV protons and carbon ions from a 3-micron laser-irradiated metallic foil are detected.

## INTRODUCTION

Since the invention of the Chirped Pulse Amplification (Strickland & Mourou, 1985), the range of accessible light intensities on focus for ultrabright lasers has only increased. Such enhancement paved the way for laser-plasma particle accelerators (LPA), mainly focused on ions (Macchi, 2013) and electrons (Esarey, 2009). The applications of such accelerated beams profit from the low-emittance and ultrashort duration of the beams, well-fitted characteristics for practical employments. Specifically, since the demonstration of collimation and monochromatisation of LPA multi-MeV ion beams (Ter-Avestiyan, 2008), their potential employments have attained plenty of attention, including fast ignition of inertial confinement fusion reactions (Roth, 2001) and medical purposes (Spencer, 2001) among others.

Due to the specific LPA beam characteristics, one of the most widely used diagnostics for laser-driven ion accelerators are Thomson Parabola spectrometers (Thomson, 1907). First developed by Thomson in 1907, they are in-line diagnostics which sort the particles depending on their energy, momentum and charge-to-mass ratio. The latter is specially useful in LPA scenario where the acceleration of multi-species beam is frequent. The main drawback of TPs is the incapability of deconvolving the spatial distribution of the measured beam as only a particular angle of the beam with an insignificant spread is evaluated because of the use of an entrance pinhole mask. Previous studies with different detectors, focused on analyzing the spatial structure of the beams, showed that the most common laser based ion acceleration mechanism, the Target Normal Sheath Acceleration or TNSA (Macchi, 2013), emits extraordinarily low-emittance beams from a source with a diameter as big as a few hundreds of micrometers and a total beam divergence of 20º. In order to retrieve spatial information about the beam other methods could be use, as stacks of radiochromic films or scintillators (Huault, 2019) which nevertheless fail when attempting to have fine spectral resolution. We present a multi-pinhole Thomson Parabola spectrometer, which combines sharp spectral and angular accuracy, besides the ionic species sorting capability.

## DESIGN

Thomson Parabola spectrometers work according to magnetic an electric sector spectrometer principle. The entrance pinhole selects a beamlet composed by ions with specific $q/m$. Parallel (or anti-parallel) magnetic ($B$) and electric ($E$) dipoles deflect the ions in orthogonal directions. Such particles are detected in a two-dimensional spatially resolved particle-sensitive detector. In paraxial approximation with perfect fields, the particles will draw a parabolic trace onto the detector (given simply by Lorentz force) as

$$y^2 = \frac{q}{m}\frac{B^2 l_2 l_3}{E}x \qquad [1]$$

where $l_2$ dipole length and $l_3$ the particle free flight distance after the deviation, being the fields parallel to the x-axis. As seen, different charge-to-mass ratio particles will describe different traces and the position of the particle onto the trace will describe its kinetic energy.

We propose a modification of the basic TP design which consist on the substitution of the entrance pinhole by a mask in which several pinholes are drilled. The array of holes chops the incoming beam into several beamlets which are simultaneously detected, resulting in a tomography-like spectral measurement with tunable spatial-resolved information (Salgado-López, 2022). Fig. 1 shows the basic device design.

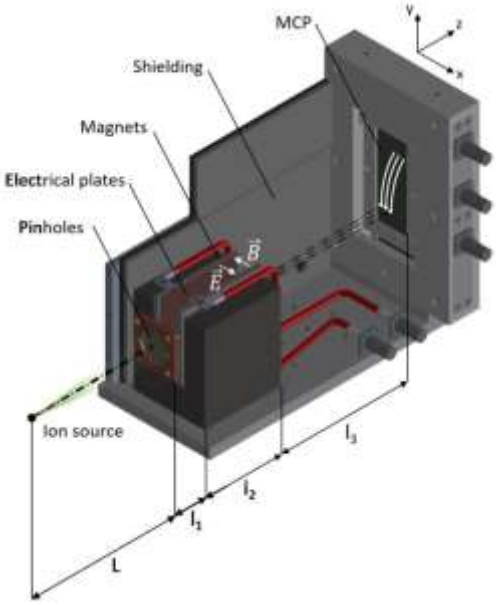


**Figure 1. Multi-pinhole TP spectrometer design.**

Previous works (Chen, 2010, Ter-Avestiyan, 2010, Yang, 2016) showed similar measurement strategies but most of the cases dismissing the electric field (and therefore the $q/m$ differentiation) or limited their detection geometries in order to avoid crossing traces on the detector (Zhang, 2018). We propose a more general approach of such device which can apply the electric and magnetic field for identifying different $q/m$ ions and measuring their spectrum at different beamlets backed by a generic post-processing method which accounts for trace crossing. A three-dimensional numerical solver was developed for trajectory simulation and provides the expected traces and the energy-position relation for the required species, which includes a Hall probe characterization of the magnetic field. In the presented configuration proton energies between 300 keV and 25 MeV are accessible; uncertainty at 20 MeV has been estimated to be around 1 MeV.

Trace crossings at the detector produce peak artifacts in the spectrum. Interpretation of such events starts with the identification of the species involved in each cross. Only artifacts producing significant distortion are treated; the peaks that are still observable after applying a Gaussian smoothing over the data are removed, by removing the relevant peak width and performing a linear interpolation between the gap edges. Such interpolation is considered to follow the data trend within its root main squared deviation.

## RESULTS

In this section we show the experimental test of the detector. Both were performed at the VEGA 3 petawatt laser facility at Centro de Láseres Pulsados (CLPU, Spain). VEGA 3 is a Titanium:Sapphire system ($\lambda$ = 0.8 μm) which delivers p-polarized pulses, up to 30 J and as short as 30 fs. The pulses are focalized by a F/11 off-axis parabolic mirror into a 10 μm full width at half maximum, which implies an averaged laser intensity over $10^{19}$ W/cm$^2$. The target was a micrometric-thick Al planar foil irradiated at 10º from the target normal in the horizontal plane.

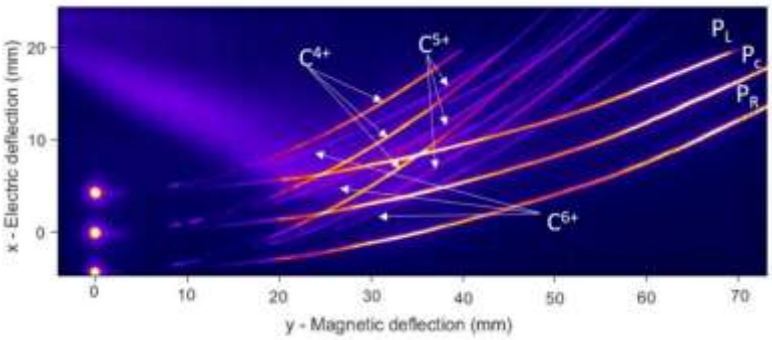


**Figure 2. Multi-pinhole TP traces from a single laser shot at VEGA 3.**

In the first commissioning test ion acceleration was detected by the multi-pinhole set at a distance from the source $L$ = 508 mm. A microchannel-plate (MCP) attached to a phosphor screen was used as active detector, which has the advantage of being well-fitted for high repetition rate (HHR) operation. As shown in fig. 2, traces were imaged onto a scientific CMOS with a calibrated imaging system. The mask in this case was made of a W substrate with $n$ = 3 drilled pinholes of $d$ = 200 μm evenly separated by $a$ = 3 mm.

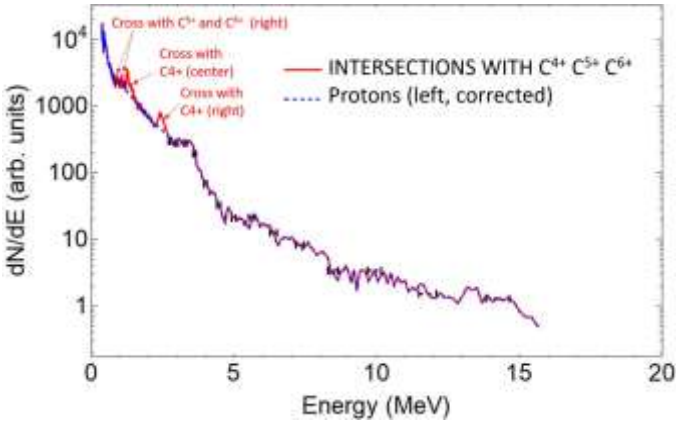


**Figure 3. Left beamlet proton (PL) spectrum from fig. 2. Dashed blue: corrected spectrum. Red: raw spectrum.**

A single beamlet proton spectrum is plotted in fig. 3, together with the traces intersection signal which are removed. In such geometrical configuration, the separation between the angles probed ($\alpha \approx a/(L) = 0.3\circ$) is small when compared to the total divergence of the beam. Therefore modest differences between different beamlet spectra are expected. Such conjecture is confirmed after the data analysis, as seen in the spectra shown in fig. 4.

## CONCLUSION

A newly developed diagnostic tool is presented. Its operation is based on the Thomson Parabola working principle and therefore able to differentiate between ionic species and presents a fine and wide spectral range of detection, which makes it well-fitted to measure characteristics of typical laser-driven ion beams. Furthermore, tomography-like measurements of the beam with varying angular resolution can be performed thanks to a mask of entrance pinholes. A post-processing method is introduced, making possible to account for trace crosses at the detector plane.

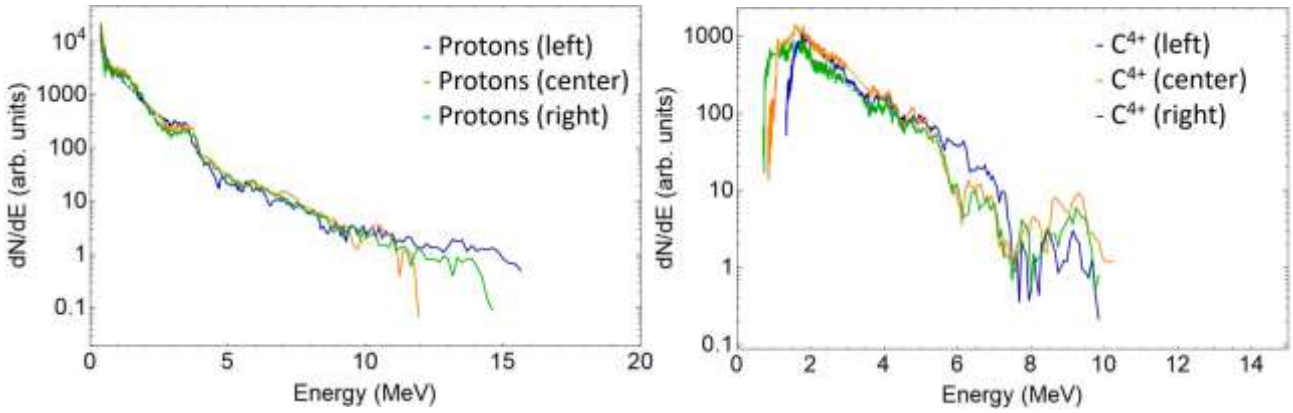


**Figure 4. Left: proton energy spectra from left, center and right beamlets (PL, PC and PR traces of fig. 2). Right: C4+ energy spectra from left, center and right beamlets of fig. 2.**

## ACKNOWLEDGMENT

Funding from LASERLAB-EUROPE V (Grant Agreement No. 871124, EU Horizon 2020 research and innovation program), IMPULSE (Grant Agreement No. 871161, EU Horizon 2020 research and innovation program) and Grant No. CLP263P20 (Junta de Castilla y León) are acknowledged.

## REFERENCES

Bolton, P. *et. al.*, (2014). Instrumentation for diagnostics and control of laser-accelerated proton (ion) beams. Physica Medica, 30: 255-270.

Chen, H. *et. al.*, (2010). An imaging proton spectrometer for short-pulse laser plasma experiments. Rev. Sci. Instrum., 81: 10D314.

Esarey, E. *et. al.*, (2009). Physics of laser-driven plasma-based electron accelerators. Rev. Mod. Phys., 81: 1129-1285.

Huault, M. *et. al.*, (2019). A 2D scintillator-based proton detector for high repetition rate experiments. High Power Laser Sci. Eng., 7.

Humphries, S. (2002). Charged Particle Beams. Jhon Wiley and Sons.

Macchi, A. and Borghesi, M. and Passoni, M. (2013). Ion acceleration by superintense laser-plasma interaction. Rev. Mod. Phys., 85: 751.

Roth, M. *et. al.*, (2001). Fast Ignition by intense laser-accelerated proton beams. Phys. Rev. Lett., 86: 433-439.

Salgado-López, C. *et al.* (2022). Angular-resolved Thomson Parabola spectrometer for laser-driven ion accelerators. Sensors, 22.

Spencer, I. *et. al.*, (2001). Laser generation of proton beams for the production of short-lived position emitting radioisotopes. Nucl. Instrum. Methods Phys. Res. Sect. B., 183: 449-458.

Strickland, D. and Mourou, G. (1985). Compression of amplified chirped optical pulses. Opt. Commun., 55: 447-449.

Ter-Avestiyan, S. *et. al.*, (2008). First demonstration of collimation and monochromatisation of a laser accelerated proton burst. Laser Part. Beams, 26: 637-642.

Ter-Avestiyan, S. *et. al.*, (2010). Tomography of an ultrafast laser driven proton source. Phys. Plasmas, 17: 063101.

Thomson, J. (1907). On rays of positive electricity. Lond. Edinb. Dublin Philos. Mag. Sci. 13: 561-575.

Yang, S. *et. al.*, (2016). A two-dimensional angular-resolved proton spectrometer. Rev. Sci. Instrum., 87: 103301.

Zhang, Y. *et. al.*, (2018). An angular-resolved multi-channel Thomson parabola spectrometer for laser-driven ion measurements. Rev. Sci. Instrum., 89: 093302.

**Return**

# Space Resolved Electron Density and Temperature Evaluation by X-Ray Pinhole Camera in ECR Plasma

G. Finocchiaro[1,2], E. Naselli[2], B. Mishra[1,2], S. Biri[3], M. Mazzaglia[2], A. Pidatella[2], R. Rácz[3], G. Torrisi[2] and D. Mascali[2]

[1] *Università degli Studi di Catania, Italy*
[2] *INFN-LNS, Catania, Italy*
[3] *ATOMKI, Debrecen, Hungary*

Email: giorgio.finocchiaro@lns.infn.it

**Abstract**

X-ray space-resolved emission characterization can provide relevant features of plasmas in terms of local distribution of electron density and temperature. In the PANDORA project framework, a high resolution full-field X-ray pin-hole setup was developed. It consists of a 400 μm hole in a lead disk coupled with a 1 MP X-ray CCD camera and a multi-layered Pb collimator. Advanced analysis techniques for single-photon-counted (SPhC) and high-dynamical-range (HDR) were developed, allowing X-ray imaging and space-resolved spectroscopy at high spatial and energy resolution (560 μm and 230 eV @ 8.1 keV respectively). We here present the first quantitative evaluation of local warm electron density and temperature of an Electron Cyclotron Resonance (ECR) Argon plasma. Thermodynamic parameters have been extracted by the analysis of the bremsstrahlung spectra, according to the theoretical emissivity model in the approximation of local Maxwell-Boltzmann distribution of electron energies. Several regions of interest (ROIs) of the image were selected, studying the space dependence of plasma parameters inside the ECR plasma volume, comparing temperature and density maps in different plasma regions. The analysis method is a powerful tool to investigate the confinement of magnetic plasmas and heating dynamics, with relevant implications about R&D of ECR Ion Sources as well as for fundamental plasma physics and nuclear physics research in these setups.

## INTRODUCTION

The main goal of PANDORA (Plasma for Astrophysics Nuclear Decay Observation and Radiation for Archaeometry) project (*Mascali D. et al., 2022*) is that of measuring β-decay lifetime variations of radioisotopes injected in a ECR plasma environment (*Geller, R., 1996).* This kind of measurements requires a good space-resolved characterization of plasma thermodynamical properties. Pinhole X-ray imaging technique is widely applied in plasma physics (*Takács, E. et al., 2005), (McPherson, L.A et al., 2016).* The setup implemented in the present work consists of a pin-hole focused CCD detector (Biri S. et al., 2021) operating in Single Photon Counting (SPhC) mode for energy-resolved acquisitions, thanks to a properly developed analysis algorithm (*Naselli E. et al., 2022*). Such system allows to characterize the X-ray fluorescence (XRF) (*Romano F. P. et al., 2014)* generated by the ionizing processes inside plasma, giving access to information about ions distribution and deconfined electron fluxes, thus allowing to study the morphologic structure of a plasma. The analysis method allowed to resolve locally the X-ray spectral information in a 2D X-ray plasma image, thus giving a map of plasma confinement dynamics. In addition, it enabled a local spectrometric investigation, which allows to indirectly measure plasma electron temperature and density. The implementation of High Dynamic Range (HDR) imaging technique was needed to investigate plasma regions with an emissivity range of several orders of magnitude. Results about the first spectrometric evaluation of local warm electron temperature and density, performed on a ECR argon plasma heated by 200 W microwave power in the 14 GHz ECR ion source of Atomki, Debrecen (*Biri S. et al., 2021*), will be described in this work.

## EXPERIMENTAL SETUP

The measurements were carried out at the ECR Laboratory of Atomki - Debrecen (*Biri S. et al., 2021*) in a B-minimum plasma trap especially designed for research aim. An argon plasma was excited in Two Close Frequency Heating mode by the injection of two pumping frequencies at 13.9

GHz and 14.25 GHz, with a total net power of 200 W. In order to study the confinement dynamics by XRF spectroscopy, a special design of the plasma chamber has been implemented: the walls were covered by different metals which generate specific fluorescence peaks, induced by the electron fluxes escaping from plasma. In particular, the lateral wall of the cylindrical chamber was covered by a Tantalum liner (E(Lα)=8.09 keV) and the extraction endplate was made in Titanium (E(Kα)=4.51 keV). The X-ray view line and the inner plasma chamber inspection was allowed through an aluminium mesh (transparency ≥ 65%), which guarantees the enclosure of microwaves resonant cavity, allowing a wide imaging field of view. FIG. 1 shows a sketch of the experimental setup, where the plasma chamber structure is reported.

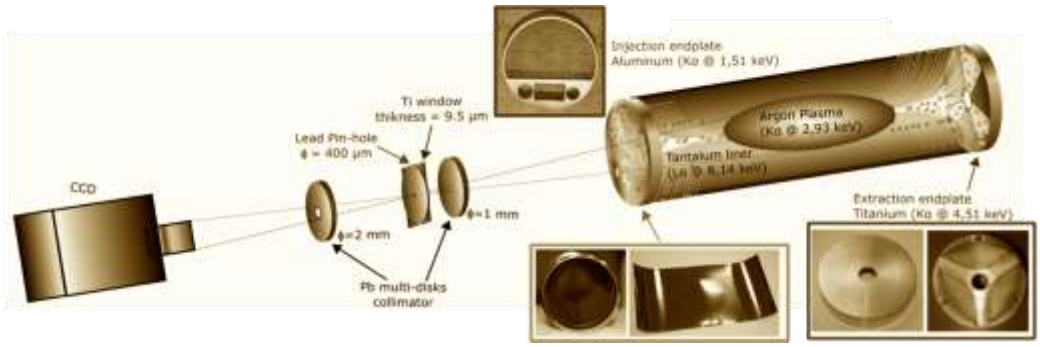


*FIG. 1 - Sketch of the experimental setup. From the left: CCD camera, pinhole multi collimator system, plasma chamber coated of tantalum liner, closed by aluminium mesh in injection endplate and titanium extraction electrode.*

The space-resolved detection of these spectral lines, together with the ones produced by the Ar ions of plasma (E(Kα) = 2.96 keV), provided a map of the X-ray emissivity.

The X-ray pin-hole camera system consists of an X-ray back-illuminated CCD (Andor, iKon-M SO series) made of 1024 × 1024 pixels (13,3 μm pixel size), sensitive in the range 0.4 - 20 keV and coupled with a 400 μm Pb pinhole, with an optical magnification M = 0.244 and a space resolution of ~560 μm. A 9.5μm Ti window was used to block visible and UV light. A specific analysis algorithm was developed (*Naselli E. et al., 2022*) for processing the SPhC output of the CCD and obtain the energy-space-resolved information. It is based on the graphic recognition of clusters of pixels activated by each single photon event, which contain the energy and position information of the impinging radiation. The SPhC condition required to set low exposure time per frame: two sets of 4000 and 1000 frames at respective exposure time of 0.5 and 0.05 seconds have been acquired to produce a single HDR energy-resolved image (Naselli E. et al., 2021).

## ENERGY-FILTERED HDR IMAGING

Spectral information was collected on each pixel, with energy resolution 230 eV at 8 keV. This information can be then re-elaborated in two ways: 1) it can be integrated over user-defined spatial ROIs, in order to obtain the relative ROI-averaged X-ray emission, or 2) it is possible to select some specific energy intervals in order to map in space the spatial distribution of detected photons corresponding, for instance, to certain characteristic X-ray lines. The overall plasma X-ray emission is mainly composed of bremsstrahlung and XRF, whose characteristic lines detection allows to perform a selective elemental imaging, thus investigating the spatial features of plasma environment. Ar, Ti and Ta filtered maps were obtained by selecting each respective energy range of the main XRF characteristic lines, in order to study the dynamics of plasma confinement (Ar) and of the axial (Ti) and radial (Ta) losses. FIG. 2 shows the total energy spectrum of plasma emission (top), the XRF map of (a) Ar (E(Kα)=2.96 keV), (b) Ti (E(Kα)=4.51 keV) and (c) Ta (E(Lα)=8.15 keV) emission. Characteristic fluorescence lines are highlighted by the same respective colors on the full-frame energy spectrum (top). Since the field of view looks through the aluminium mesh of the injection flange, the plasmoid and the extraction flange on the opposite side are well visible in the pictures. All the images are affected by the “shadow” of the aluminium mesh

(400 μm wire) along the line of view, which creates the well visible regular pattern as an intensity modulation.

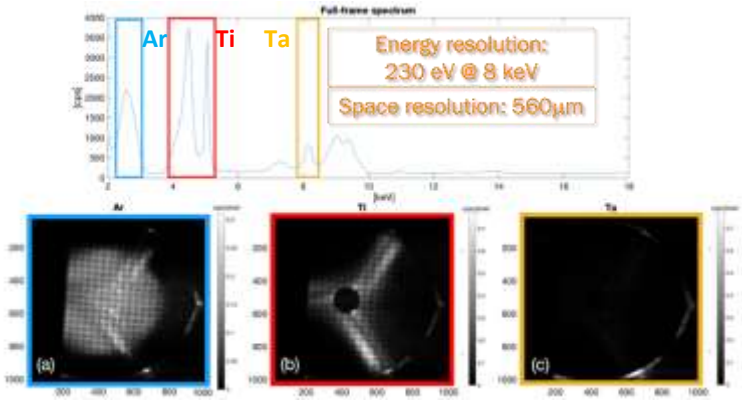


*FIG. 2 – Total energy spectrum (top) - Images filtered in the emission of argon (a), titanium (b) and tantalum (c). Characteristic fluorescence lines are highlighted on the spectrum with the same colors of respective images.*

The plasmoid, the extraction flange and the chamber walls are well visible in the pictures with a spatial resolution of 560 μm, calculated at the center of plasma chamber. The quasi-circular cross-section of the plasmoid, well visible in FIG. 2-(a), well depicts the expected ellipsoidal cross-section of the ECR surface, defined by the magnetic isosurface corresponding to the cyclotron resonance. The tri-cuspidal structure, visible in FIG. 2-(b), corresponds to the footprint of axially deconfined plasma electrons impinging on the titanium plate, mostly determined by the shape of the confining hexapolar magnetic field at the intersection with the plate (see also FIG. 1, bottom-right). In FIG. 2-(c) the same effect is visible in the tantalum lateral wall of the plasma chamber.

## ELECTRON DENSITY AND TEMPERATURE EVALUATION

According to a model of plasma emissivity (*Mishra B. et al., 2021*), it is possible to extrapolate the plasma thermodynamic parameters from the experimental emissivity density distribution $J_{exp}$, defined by the equation:

$$J_{exp}(h\nu) = h\nu \frac{N^{p}(h\nu)}{t} \frac{4\pi}{\Delta E V_P \Omega_g} \qquad (1)$$

where $h\nu$ is the photon energy, $N^P(h\nu)/t$ is the measured counting rate energy spectrum, $\Delta E$ is the energy bin width, $V_P$ the plasma volume and $\Omega_g/4\pi$ the geometrical efficiency. Such quantity is mainly composed by the XRF and bremsstrahlung emission. The Kramer cross-section formula, assuming a Maxwell-Boltzmann Electron Density Distribution Function (EEDF) (*Mishra B. et al., 2021*), defines the bremsstrahlung emissivity density, described by the equation:

$$J^{M-B}_{bremss}(h\nu) = \rho_e \rho_i (Z)^2 \sqrt{\frac{4\pi}{6m_e}} \sqrt{\frac{3}{k_B T_e}} e^{-\frac{h\nu}{k_B T_e}} \qquad (2)$$

where $\rho_e\rho_i$ is the product of the electron and ion density, $k_B$ is the Boltzmann constant and $T_e$ the electron temperature. This expression can be used to fit the bremsstrahlung experimental emissivity density, obtained by the continuous part of the energy spectra, to extrapolate the electron temperature and density. A simulation is required to evaluate the emission volume $V_P$ and the geometrical detection efficiency $\Omega_g/4\pi$ in each point of the plasma, considering the overall geometry of the pin-hole optical system and the plasma chamber setup. The total plasma volume is identified as the region enclosed by the ECR surface, defined by the 3D-map of the resonant magnetic region. The geometrical efficiency has been defined in all the plasma volume as the projection of each point of plasma across the aluminium mesh and the pinhole into the CCD detector. FIG. 3 shows the aluminium mesh (a), the optical simulation of plasmoid through it (b) and the geometrical efficiency projection along the z axis (c). A set of ROIs, shown in Figure 4-(left), has been defined to study the emissivity density in several plasma regions. Each of them defines a 3D portion of plasma on which the volume V and the efficiency $\Omega_g/4\pi$ are summed.

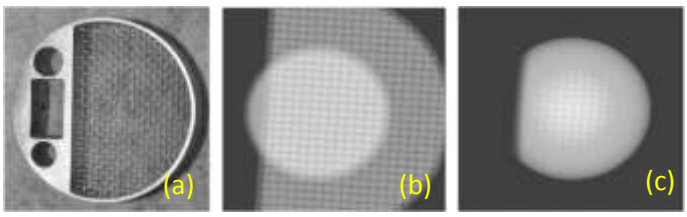


*FIG. 3 – (a) Aluminium mesh mounted along the line of view, (b) optical simulation of plasma view through the mesh, (c) geometrical detection efficiency projection along the z axis.*

The emissivity density is defined in each ROI by summing the energy spectra contained into the respective area. FIG. 4 – (right) reports the extrapolated values of temperature and density in all the 4 ROIs, with their respective error bars, calculated by the experimental error propagation into the fit parameters. Being the experimental error mostly dependent on the spectrum intensity, the measurement can be in principle improved by extending the total measurement time and/or increasing the spatial ROI dimensions, in a trade-off between parameters extrapolation accuracy, measurement time and space resolution of the method.

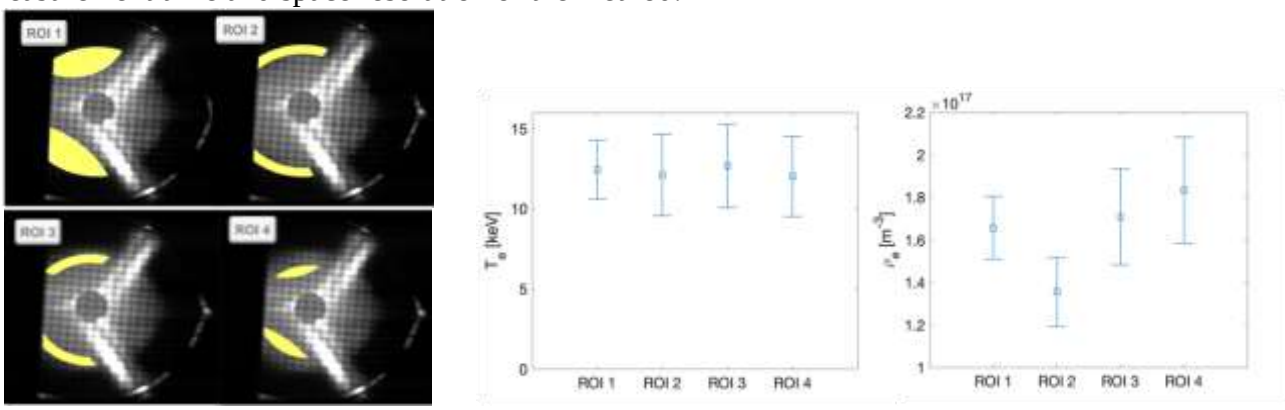


*FIG. 4-(Left) - Images obtained by the sum of all the three energy-filtered components (shown in FIG. 2-(a)-(b)-(c)) where the set of ROIs on the CCD image are highlighted in yellow. (Right) - Respective electron temperature and density results.*

## CONCLUSION

We reported the first experimental results of local plasma parameters evaluated by a CCD-based pin-hole camera for X-ray spectroscopy and imaging. Energy-resolved imaging makes possible the study of elemental space distribution, giving information about plasma structure and confinement dynamics with a space resolution of 560 µm and energy resolution of 230 eV at 8 keV. Local plasma parameters evaluation was obtained from the bremsstrahlung component of the acquired spectra with an accuracy of ~ 10% - 25%, under the assumption of Maxwell-Boltzmann EEDF distribution.

## ACKNOWLEDGMENT

The authors gratefully acknowledge the support of INFN by the Grants PANDORA (5th Nat. Comm.) and PANDORA_Gr3 (3rd Nat. Comm.).

## REFERENCES

*Geller, R. (1996) Electron Cyclotron Resonance Ion Sources and ECR Plasmas.*
*Takács, E. et al., (2005) Nucl. Instrum. Meth. B, 235, 120-125.*
*Romano F. P. et al. (2014) Anal. Chem. 86, 21, 10892–10899.*
*McPherson, L.A et al. (2016) Rev. Sci. Instrum., 87, 063502.*
*Biri S. et al. (2021) Eur. Phys. J. Plus, 136, 247.*
*Naselli E. et al. (2021) J. Instrum, 17, C01009.*
*Mishra B. et al. (2021) Phys. Plasmas. 28 102509.*
*Mascali D. et al. (2022). Universe **8(2)**, 80.*
*Naselli E. et al. (2022) Condens. Matter, 7, 5.*

**Return**

# 1D SPACE-TIME & 2D SPACE RESOLVED HOT ELECTRON GENERATION AT SHOCK IGNITION RELEVANT PARAMETERS

Renner, O[1,2,3], Batani, D[4], Cristoforetti, G[5], Červeňák, M[2], Dudžák, R[1,2], Filippov, E[6], Gajdoš, P[2], Gizzi, LA[5], Juha, L[1], Korneev, Ph[7], Koester, P[5], Krůs, M[2], Martynenko, A[8], Nicolai, P[4], Pikuz, S[6], Pisarczyk, T[9], Singh, S[1,2], Tentori, A[4], Tikhonchuk, VT[3,4], and Weber, S[3]

[1]Institute of Physics, Czech Academy of Sciences, Prague, Czech Republic
[2]Institute of Plasma Physics, Czech Academy of Sciences, Prague, Czech Republic
[3]Extreme Light Infrastructure ERIC, ELI Beamlines Facility, Dolní Břežany, Czech Republic
[4]Université Bordeaux, CNRS, CEA, CELIA, Talence, France
[5]National Institute of Optics, CNR-INO, Pisa, Italy
[6]Joint Institute of High Temperature of RAS, Moscow, Russian Federation
[7]P.N. Lebedev Physical Institute of RAS & MEPHI, Moscow, Russian Federation
[8]IGSI Helmholtzzentrum für Schwerionenforschung GmbH, Darmstadt, Germany
[9]Institute of Plasma Physics and Laser Microfusion,Warsaw, Poland
renner@fzu.cz

**Abstract**

The kinetics of hot electron (HE) generation accompanying intense laser-matter interaction, detailed mechanisms of their production, and impact on formation of strong shocks and magnetic fields are not fully understood yet. The aim of experiments conducted at the Prague PALS laser facility is to collect precise data needed for development of theoretical models describing the HE formation, transport, and energy deposition inside targets which affect the shock dynamics. Here we report on x-ray measurements characterizing HE generation via 1D space-time and 2D space-resolved imaging of HE-induced Kα emission inside the cold target material. The experiments were performed at laser intensities up to $2\times10^{16}$ W/cm$^2$, i.e., at parameters of the laser-plasma coupling suitable to address the physics of the laser spike induced shock wave igniting the fusion reaction. We describe the experimental setup and provide examples of HE records observed at different geometry targets.

## INTRODUCTION

The interaction of high intensity laser radiation with solid targets is accompanied by strongly nonlinear phenomena. Despite a progress in theoretical description of relevant processes (Batani et al, 2019, Tikhonchuk, 2019), the laser energy deposition into the target is not fully understood even at moderate intensities $10^{15}$ - $10^{16}$ W/cm$^2$. Here the laser energy deposition switches from collisional absorption to mechanisms governed by resonance excitation of large-amplitude plasma waves, namely by stimulated Brillouin (SBS) and Raman (SRS) scattering and two plasmon decay (TPD). In longer scale-length plasmas, these parametric instabilities dominate the generation of hot electrons (hereafter HE) compared to alternate processes, e.g., resonant absorption and vacuum heating.

The detailed investigation of HE production is of paramount interest for fundamental research in the fields of laboratory astrophysics and in general high-energy-density physics (Renner & Rosmej, 2019). The more practical applications refer to the HE role in implementation of diverse scenarios for inertial confinement fusion (ICF). The research reported here belongs to a series of experiments conducted at the PALS laser facility (Jungwirth et al, 2001) at intensities up to $2\times10^{16}$ W/cm$^2$, i.e., at parameters of the laser-plasma coupling suitable to address the physics of the shock ignition scheme (Batani et al, 2019). The HE generation is characterized via 2D space- and 1D space-time resolved imaging of the HE-induced Cu Kα emission from the target. The 2D resolved data determine the HE dose and spatial distribution, the 1D space-time resolved images corelate the HE evolution with the temporal laser profile. The precisely measured data provide an input needed for benchmarking of novel theoretical approaches to complex modeling of the parametric instabilities

growth, HE production and transport in partially ionized targets (Tentori et al, 2022).

**EXPERIMENT**

The experiments were performed using the fundamental frequency radiation of the PALS iodine laser (1315 nm, 0.3 ns, ≤600 J). The random phase plate smoothed beam was focused to a focal spot with a FWHM diameter of 100 μm. The detailed description of the experimental complex, as well as a survey of results obtained can be found in papers (Pisarczyk et al, 2018 & 2022, Cristoforetti et al, 2021, Filippov et al, 2023). Here we focus on 2D space and 1D space-time resolved investigation of HE generation via imaging of the HE-induced Kα emission from Cu-containing targets.

The principle of imagers based on spherically bent crystals can be found e.g. in (Renner & Rosmej, 2019). The HEs accompanying the laser-matter interaction collide with inner-shell electrons of Cu which results in 2p → 1s fluorescence. The coincidence between the Cu $K\alpha_1$ wavelength (1.5406 Å) and the 2*d* interplanar spacing (1.5414 Å) of the spherically bent quartz (422) crystal results in quasi-normal diffraction from the crystal. The novelty of our approach consists in absolute calibration of the imaging system via detailed ray tracing (Podorov et al, 2001) which is of paramount importance for quantitative interpretation of 2D resolved images and/or, in a combination with the Hamamatsu high dynamic range x-ray streak camera (XSC), for optimized measurements of temporal corelation between HE-induced signals and the laser profile in case of the 1D space-time resolved imaging.

The experimental setup is depicted in Figure 1. For 2D imaging, both the crystal and the detector are fielded inside the interaction chamber which provides more freedom in a choice of the experimental configuration. In 1D case, the XSC is fixed onto one of the chamber flanges which defines the distance c between the target and XSC slit, thus the system magnification M=b/a and the crystal position are strictly determined. For 2D and 1D systems, the crystals with radii of 380 and 500 mm provided M = 1.7 and 3.96 and the spectral window of approximately 0.8 and 1.4 mÅ. This is sufficient to cover the Cu $K\alpha_1$ emission (with the FWHM width of 0.4 mÅ) from the cold Cu but cuts off the $K\alpha_2$ component and the frequency shifted Kα emission from the heated target (Renner et al, 2016). The ray traced transfer function of imagers related 1 Cu $K\alpha_1$ photon emitted from the source into the full solid angle to $\sim 1.3\times10^{-6}$ and $8.9\times10^{-7}$ photons incident on the detector, respectively.

The spatial resolution of the 2D imager recalculated to the target plane was limited by the signal spreading in the IP used (Fuji MS and SR type) to about 30 μm. In 1D imaging scheme optimized for meridional diffraction, the Cu Kα1 image was projected onto the XSC entrance slit with dimensions of 18 mm × 80 μm (space × time resolving direction). In this case, the spatial resolution corresponds to about 4 μm. With respect to the sweeping speed used (average value 5.35 ps/px), the temporal smearing of the recorded signal equals to approximately 33 ps. The absolute temporal calibration of the HE-induced Cu $K\alpha_1$ profiles was provided via a frequency tripled fiducial split-off from the main laser beam brought onto the XSC slit. The observed variable spacing between the fiducial and the time-space resolved image of the HE action was then used to determine the absolute temporal delay between the laser profile and the time-resolved HE signal. More details about the 1D space-time resolved HE-induced Cu Kα imaging will be published elsewhere (Renner et al, 2023).

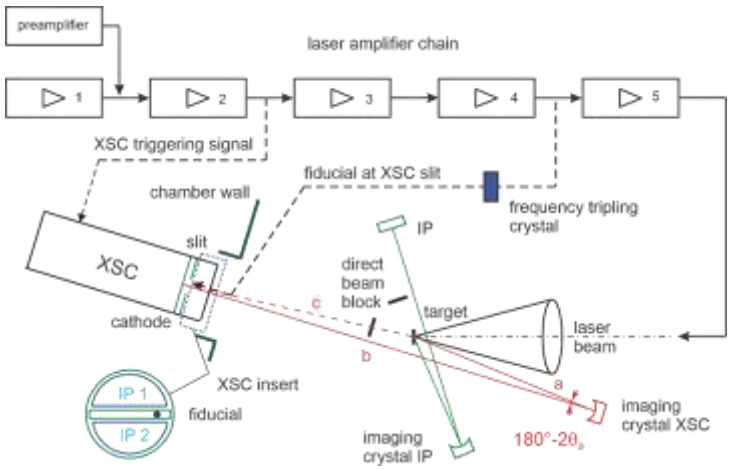


**Figure 1. A scheme of the imaging system combining the spherically bent crystal diffractors with time resolving (x-ray streak camera, XSC) or time integrating (imaging plate, IP) detectors.**

## RESULTS AND DISCUSSION

The diagnostic potential of the described methods is illustrated on several examples of 2D and 1D space-time-resolved imaging of HE generation in Cu-containing targets. Both records presented in Fig. 2 relate to investigation of magnetic fields produced at laser irradiated targets. Figure 2a indicates the HE energy deposition in the snail-shape target. The HE interaction peaks near the shallow-angle laser impact close to the snail entrance but slowly decays along its whole internal surface. This long interaction length leads to a very efficient laser energy deposition in the target affecting the magnetic field formation. The full dose of created HEs was estimated by using the GEANT4 code (Agostinelli et al, 2003) to 1.5 J. Details of this methodology are presented in the paper Pisarczyk et al (2018).

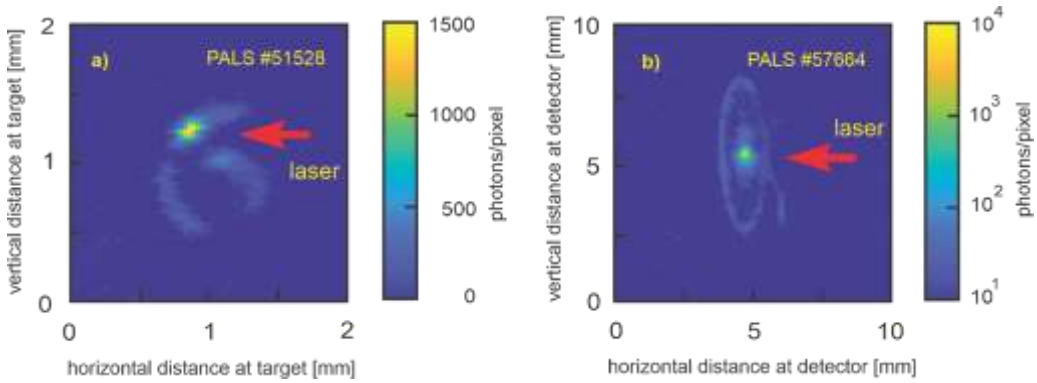


**Figure 2. Hot electron deposition along the surface of the laser irradiated snail-shape target (a) and in the disc target connected to the coil (b).**

Figure 2b bears upon optical generators of strong magnetic fields based on the laser driven coil-target concept. The 50-µm-thick Cu disk coupled to a grounded single-turn coil was irradiated by the laser beam with an energy of 500 J. The experiment aimed at investigation of the coil-induced magnetic field effect on the ablative plasma, in particular on generation of HEs and ions responsible for transport of the laser energy to the shock wave. The experimental data proved that the presence of the axial magnetic field leads to an increased collimation of HE fluxes and to enhanced production of higher-energy HEs, i.e., to the increased laser energy conversion to HEs (Pisarczyk et al, 2022).

The examples of the time resolved measurements of the HE generation in bare Cu and structured targets with Cu tracing layer are presented in Fig. 3. Temporal correlation of the HE induced Cu $K\alpha_1$ emission with the laser beam irradiating the massive Cu target is shown in Fig. 3a. The rising edge of the HE signal is delayed by 86±45 ps vs that of the laser profile, the HE maximum lags behind the laser by 19±45 ps. In contrast, the rising edge of the HE production observed at composite targets with Al ablator practically coincides with the laser profile and the HE maximum even precedes that of the laser, see Figure 3b. This behavior reflecting the diverse kinetics of the

HE generation at targets with different atomic numbers agrees with conclusions of CHIC code modeling (Llor Aisa et al, 2017) but a conclusive interpretation of observed phenomena should be confirmed by advanced simulations.

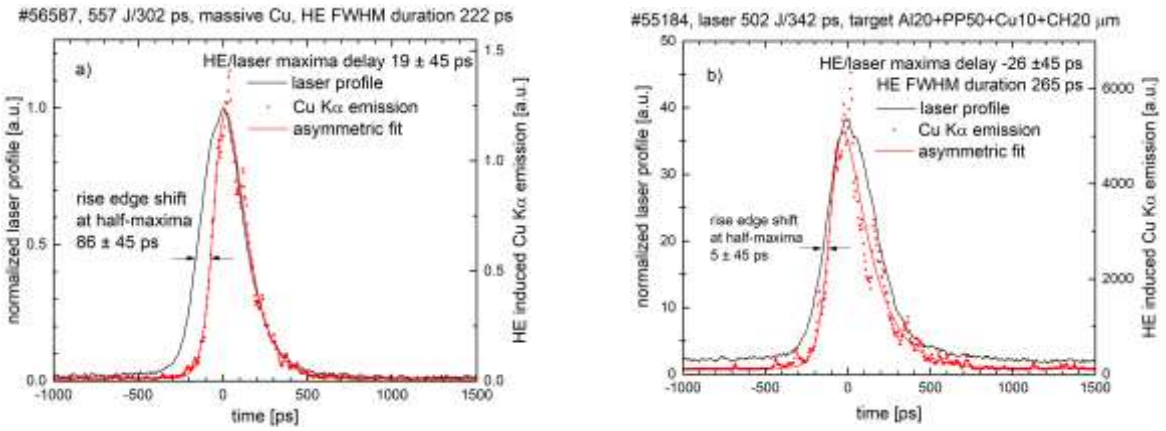


**Figure 3. Time resolved hot electron emission from the massive Cu target (a) and the structured target with the Al ablator and the Cu tracing layer (b) absolutely calibrated vs the plasma producing laser beam.**

## CONCLUSION

The 1D space-time and 2D space resolved methods of x-ray imaging based on measurements of the HE-induced K-shell emission from the laser irradiated targets containing Cu atoms are capable of providing direct information on fundamental properties of the produced HEs including their formation temporally related to the laser profile, energy deposition and transport in the target material. The understanding of these characteristics and processes connected with the HE generation contributes to a detailed interpretation of diverse phenomena accompanying the laser-matter interaction and, in particular, to the practical realization of one of the ICF scenarios.

## ACKNOWLEDGMENT

The authors acknowledge a support of the PALS Infrastructure within the MŠMT (MEYS) project No. LM2023068. This work has been carried out within the framework of the EUROfusion Consortium, funded by the European Union via the Euratom Research and Training Programme (Grant Agreement No 101052200 — EUROfusion). Views and opinions expressed are however those of the authors only and do not necessarily reflect those of the European Union or the European Commission. Neither the European Union nor the European Commission can be held responsible for them. The involved teams have operated within the framework of the Enabling Research Project: ENR-IFE.01.CEA “Advancing shock ignition for direct-drive inertial fusion".

## REFERENCES

Agostinelli S. et al (2003). GEANT4 simulation toolkit. Nucl. Instr. Methods Phys. Res., A 506: 250.

Batani D. et al (2019). Progress in understanding the role of hot electrons for the shock ignition approach to inertial confinement fusion. Nucl. Fusion, 59: 032012.

Cristoforetti G. et al (2021). Observation and modelling of stimulated Raman scattering driven by an optically smoothed laser beam in experimental conditions relevant for Shock Ignition. High Power Laser Sci. Eng. 9: e60.

Cristoforetti G. et al (2023). Investigation on hot electron origin in laser plasma interaction at Shock Ignition intensities. (in preparation).

Filippov E.D. et al, (2023) Characterization of hot electrons generated by laser-plasma interaction at shock ignition intensities., Submitted to Matter Radiat. Extremes.

Jungwirth K. et al (2001). The Prague Asterix Laser System PALS. Phys. Plasmas, 8:2495.

Llor Aisa E.L. et al (2017). The role of hot electrons in the dynamics of a laser-driven strong converging shock. Phys. Plasmas 24: 112711.

Pisarczyk T. et al (2018). Magnetized plasma implosion in a snail target driven by a moderate intensity laser pulse. Sci. Reports, 8: 17895.

Pisarczyk T. et al (2022). Influence of the magnetic field on properties of hot electron emission from ablative plasma produced at laser irradiation of a disc-coil target. Plasma Phys. Control. Fusion, 64: 115012.

Podorov S.G. et al (2001). Optimized polychromatic x-ray imaging with asymmetrically bent crystals. J. Phys. D: Appl. Phys. 34: 2363.

Renner O. et al (2016). Suprathermal electron production in laser-irradiated Cu targets characterized by methods of x-ray imaging and spectroscopy. Plasma Phys. Control. Fusion 58: 075007.

Renner O. and Rosmej F.B. (2019). Challenges of x-ray spectroscopy in investigations of matter under extreme conditions. Matter Radiat. Extremes, 4: 024201.

Renner O. et al (2023). Time resolved x-ray imaging of hot electron generation at shock ignition relevant laser-target coupling parameters. (in preparation).

Tikhonchuk V.T. (2019). Physics of laser plasma interaction and particle transport in the context of inertial confinement fusion. Nucl. Fusion, 59: 032001.

**Return**

# COHERENT XUV MULTISPECTRAL DIFFRACTION IMAGING IN REFLECTION MODE AND PROSPECT IN DENSE PLASMA DIAGNOSTICS

E.P. Benis[1,2], S. Petrakis[1,2], A. Skoulakis[1], Y. Orfanos[1], N. Kortsalioudakis[3], C. Balas[3], D. Zouridis[4], E. Pachos[4], M. Bakarezos[1], V. Dimitriou[1], M. Tatarakis[1], and N.A. Papadogiannis[1]

[1]*Institute of Plasma Physics and Lasers, Hellenic Mediterranean University Centre for Research & Innovation, 74100 Rethymno, Greece*

[2]*Department of Physics, University of Ioannina, 45110 Ioannina, Greece*

[3]*School of Electrical & Computer Engineering, Technical University of Crete, 73100 Chania, Greece*

[4]*IKNOWHOW (IKH), 340 Kifisias 116 Ave. Neo Psychiko, 15451 Athens, Greece*

E-mail: mbenis@uoi.gr

**Abstract**

Current science and related technology of optical dynamic imaging in the nanoscale requires a spatiotemporal resolution offered by coherent ultrafast radiation with wavelengths reaching the x-ray region. Lensless coherent diffraction imaging is a powerful tool towards such studies, especially when used in reflection mode, appropriate for the characterization of micro- and nano-structures developed on surfaces, as well as for dense plasma diagnostics. In this article, we present the feasibility of multispectral coherent diffraction imaging in reflection mode in the extreme ultraviolet, demonstrating that features of the order of a few hundreds of nanometers can be resolved. The coherent extreme ultraviolet radiation used consists of a comb of high harmonics generated by near-infrared femtosecond laser pulses focused onto an atomic gas target, while the selection of specific extreme ultraviolet harmonics is performed by specially designed pairs of multilayer mirrors.

## 1. INTRODUCTION

The spatiotemporal resolution of optical dynamic imaging depends on the wavelength and duration of the radiation in use. Current needs drive science and related technology towards its limits using ultrafast radiation with wavelengths reaching the x-ray region. To fully exploit the advantages of such small wavelengths, the radiation must be coherent. Ultrafast coherent XUV and x-ray radiation can be generated either by large and expensive synchrotrons and free-electron lasers, or by table-top systems via femtosecond (fs) laser high harmonics (HH) (Lewenstein et al., 1994). Lensless coherent diffraction imaging (CDI) has been proven as the favorable technique in the XUV and x-ray spectral regions (Sandberg et al., (2007), Zurch et al., (2014), Miao et al., (2015), Gardner et al., (2017)). Table-top HH systems are suitable for high quality ultrafast CDI, since the produced XUV radiation has high coherence and adequate intensity, while the ultrafast properties and phase front are preserved. Since XUV wavelengths have a very small penetration depth, CDI in reflection mode is required for the characterization of micro- and nano-structures developed on surfaces as well for dense plasma diagnostics, not applied to so far. Besides the high

spatiotemporal resolution, CDI XUV HH systems offer a comb of wavelengths that can be utilized for multispectral imaging. In our recent article (Petrakis et al., 2022b), we have shown that the use of a combination of multilayer mirrors allows for the selection of specific wavelengths which have been used for XUV CDI in transmission mode. CDI in reflection mode has the added complexity that the XUV radiation must be incident onto the sample at grazing angles, for which the reflected diffraction energy is sufficiently large.

In this article, we present multispectral XUV CDI in reflection mode of the honeycomb structure of a commercially available multichannel plate (MCP), demonstrating that features of the order of a few hundreds of nanometers can be resolved. We have compared imaging results for three different wavelengths, namely 807 nm, 46.7 nm, and 32.2 nm. Whereas with the 807 nm wavelength the honeycomb structure features cannot be accurately resolved, the 32.2 nm is found to offer higher resolution than the 46.7 nm wavelength.

## 2. MATERIALS AND METHODS

The optical layout of the XUV CDI experimental setup operating in reflection mode is shown in figure 1. The setup was designed and developed at IPPL-HMU (Clark et al., 2021), and was largely based on our XUV CDI setup in transmission geometry, described in detail in (Petrakis et al., 2022b). The coherent XUV radiation is generated as a comb of HH after focusing the IR laser pulses, delivered by the Ti:Sa laser system with a central wavelength of 807 nm, energy per pulse of 1 mJ and a minimum pulse duration of 26 fs, at the exit of the semi-infinite cell filled with a gas target. The XUV beam propagates along with the residual IR laser beam to the wavelength selection stage of the setup. First, a filtering of the residual IR laser beam is done using a 400 nm thick Al filter. Then, the selection of the wavelengths is done via two pairs of mirrors, each consisting of a multilayer flat mirror and a multilayer spherical concave mirror. Each pair of multilayer mirrors reflects only a narrow band (~2 nm) around the central wavelengths of 46.7 nm and 32.2 nm. The pairs of multilayer mirrors are placed on a movable platform that is externally controlled, thus offering the option of wavelength selectivity by simply exchanging the pairs of mirrors during measurements. The selected part of the XUV spectrum can be optimized with respect to the gas species and pressure in use, the location of the laser focus, and the chirp of the laser pulses (Petrakis et al., (2021), Petrakis et al., (2022a), Petrakis et al., (2022b)). The spherical mirror, having a radius of curvature of 1000 mm, focuses the selected XUV beam onto the object under study. The monochromatic coherent XUV radiation diffracted by the surface of the object is recorded by a 16-bit XUV vacuum CCD camera, with a sensor of 1024x1024 pixels (13.3 μm/pixel), located 41.7 mm after the object. The object used for the CDI studies was the honeycomb structure of a part of a MCP having a channel diameter of 10 μm and a distance between two channels of 12 μm. The object was placed at the focus of the XUV beam at a grazing incident angle of 13.9$^{o}$ with respect to the k-vector of the XUV beam.

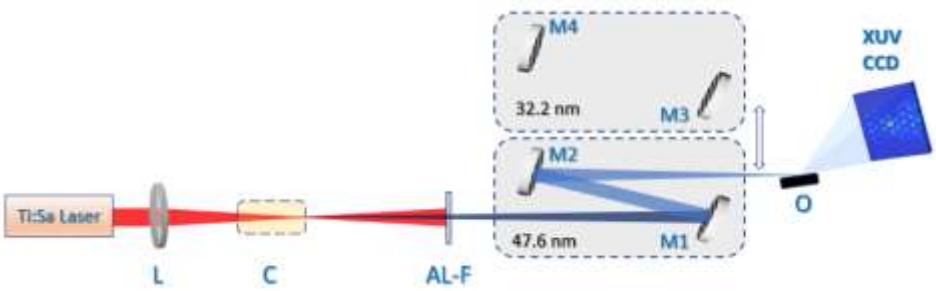

**Figure 1. The optical layout of the XUV CDI experimental setup operating in reflection mode. L: Lens. C: Semi-infinite gas cell. AL-F: Aluminum filter. M1, M3: Flat multilayer mirrors. M2, M4: Concave spherical multilayer mirrors. O: Object.**

## 3. RESULTS AND DISCUSSION

Initially, we employed simulations to derive the expected diffraction pattern based on the optical geometry of our XUV CDI in reflection mode setup. Thus, we used an artificial honeycomb structure, similar to that of the MCP in use, and rotated it by 76.1$^{o}$ with respect to the honeycomb surface normal. The rotation of the object results in a geometrical shortening along the illumination direction, as shown in figure 2a. The simulated diffraction pattern is presented in figure 2b. Figure 2c shows the reconstructed object taking into account the 76.1$^{o}$ rotation. In the same figure, the honeycomb structure is shown overlapped with the reconstructed object for comparison. This analysis clearly shows that the reconstructed object consists of bright spots located at the center of the honeycomb MCP channels. Therefore, the reconstruction of the real object in our experiments using the two XUV wavelengths is expected to follow a similar pattern.

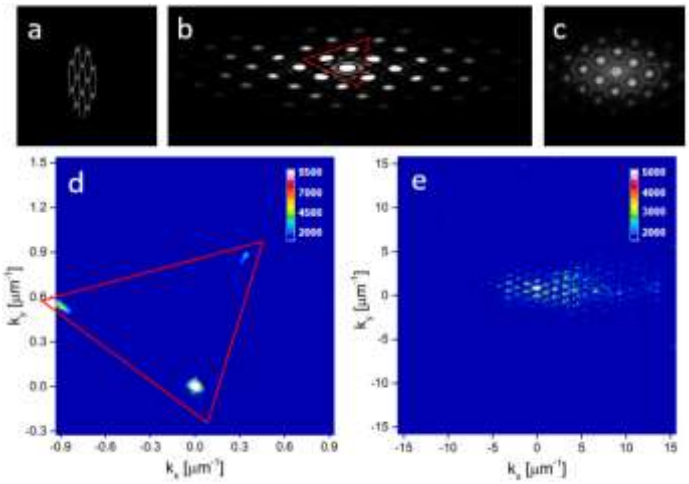


**Figure 2. (a) Schematic of a MCP honeycomb object rotated by 76.1$^{o}$ to match the experimental viewing angle by the illuminating XUV beam. (b) The simulated diffraction pattern of (a). (c) The geometry-corrected reconstruction overlapped with the original MCP honeycomb object. (d) Experimentally recorded CDI image from the real MCP honeycomb object for a wavelength of 807 nm. (e) Same as in (d) but for a wavelength of 47.6 nm.**

In Figure 2d the measured diffraction image obtained using the fundamental laser beam with a wavelength of 807 nm is shown. Only three diffraction spots are recorded on the CCD camera sensor, contained inside a red triangle that corresponds to the red triangle of the diffraction pattern of figure 2b. In figure 2e, a typical XUV diffraction pattern using the 47.6 nm wavelength is shown. Within the XUV CCD sensor, a high order diffraction pattern is recorded similar to that of the simulation in figure 2b.

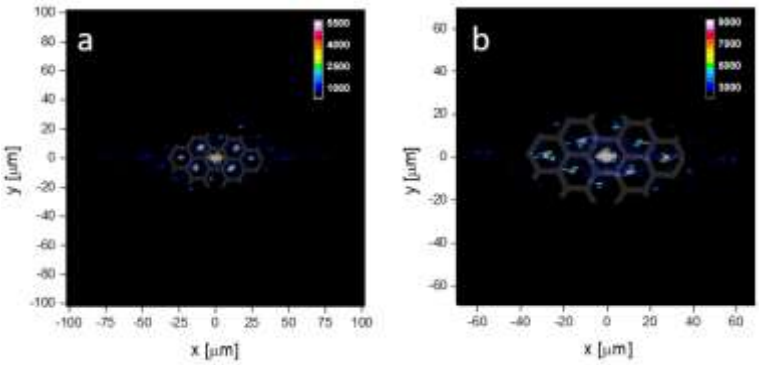

**Figure 3. (a) Geometry-corrected reconstruction of the honeycomb MCP object using the XUV beam with a wavelength of 47.6 nm. (b) Same as in (a) but for a wavelength of 32.2 nm. The overlapped honeycomb pattern is a guide to the eye and corresponds to the actual MCP channel dimensions.**

In Figures 3a,b the geometry-corrected reconstruction of the real MCP honeycomb object is presented, for 47.6 nm and 32.2 nm, respectively. The reconstructions of the object were developed using the RAAR algorithm (Luke et al., 2005), with a workflow structure similar to the one described in detail in our recent work on transmission XUV CDI (Petrakis et al., 2022b). As a guide to the eye, a honeycomb pattern with the same area of the object, scaled to the actual MCP channel dimensions, is overlapped to the reconstructed images. It must be mentioned that in figures 3a,b, each pixel corresponds to 200 nm and 140 nm, respectively, based on the analysis presented in (Dilanian et al., (2009), Prosekov et al., (2021)). As in the case of the artificial honeycomb structure, the reconstruction of the real MCP object consists of bright spots located at the centers of the MCP channels. Comparing the reconstruction in figures 3a,b, it is evident that the object is 1.5-times larger for 32.2 nm as compared to 47.6 nm, reflecting the inverse ratio of the wavelengths. Furthermore, using the shorter wavelength of 32.2 nm, object features can be resolved with a higher resolution since a higher number of pixels corresponds to the same bright spot areas.

Multispectral XUV CDI in reflection mode could be proven a powerful tool for spatiotemporal imaging of the evolution of the critical plasma density front, especially for the case where a high power laser illuminates a solid surface. Oscillating high crtitical density plasma surfaces are the mechanism for the relativistic high harmonic generation (Nomura et al., 2009). In this framework, ultrafast and high spatial resolution imaging of the critical plasma density evolution could be a unique tool for understanding the underlying physical mechanisms.

## 4. CONCLUSION

In this article we have demonstrated multispectral XUV CDI in reflection mode of the surface of a MCP honeycomb structure. Our system is based on a versatile table-top high harmonic generation source where amplified fs IR laser pulses are focused onto atomic gas targets. The combination of appropriate XUV optics, such as specially designed multilayer mirrors, grazing incidence geometry, and reconstruction algorithms, allowed us to demonstrate that multispectral reflection CDI in the XUV is feasible. Prospects for using multispectral XUV CDI in dense plasma diagnostics have been discussed.

## 5. ACKNOWLEDGMENT

This research was co-financed by the European Regional Development Fund of the European Union and Greek national funds through the Operational Program Competitiveness, Entrepreneurship and Innovation, under the call RESEARCH—CREATE—INNOVATE (project code: T1EDK-04549, project title: Development of a coherent X-ray multispectral microscopy system).

## 6. REFERENCES

Clark, E.L. et. al., (2021). High-intensity laser-driven secondary radiation sources using the ZEUS 45 TW laser system at the Institute of Plasma Physics and Lasers of the Hellenic Mediterranean University Research Centre. High Power Laser Sci. Eng., 245: 9, e53.

Dilanian et. al., (2009). Diffractive imaging using a polychromatic high-harmonic generation soft-x-ray source. J. Appl. Phys., 106: 023110.

Gardner, D.F. et. al., (2017). Subwavelength coherent imaging of periodic samples using a 13.5 nm tabletop high-harmonic light source. Nat. Photon., 11: 259–263.

Lewenstein, M. et. al., (1994). Theory of high-harmonic generation by low-frequency laser fields. Phys. Rev. A, 49: 2117–2132.

Luke, D.R. (2005). Relaxed averaged alternating reflections for diffraction imaging. Inverse Problems, 21: 37–50.

Miao, J., et. al., (2015). Beyond crystallography: Diffractive imaging using coherent x-ray light sources. Science, 348: 530–535.

Nomura, Y., et. al., (2009). Attosecond phase locking of harmonics emitted from laser-produced plasmas. Nat. Phys., 5: 124–128.

Petrakis, S., et. al., (2021). Electron quantum path control in high harmonic generation via chirp variation of strong laser pulses. Sci. Rep., 11: 23882.

Petrakis, S., et. al., (2022a). Spectral and divergence characteristics of plateau high-order harmonics generated by femtosecond chirped laser pulses in a semi-infinite gas cell. Atoms, 10: 53.

Petrakis, S., et. al., (2022b). Coherent XUV multispectral diffraction imaging in the microscale. Appl. Sci., 12: 10592.

Prosekov, P.A., et. al., (2021). Methods of coherent x-Ray diffraction imaging. Crystallogr. Rep., 66: 867–882.

Sandberg, R.L., et. al., (2007). Lensless diffractive imaging using tabletop coherent high-harmonic soft-x-ray beams. Phys. Rev. Lett., 99: 098103.

Zurch, M., et. al., (2014). Real-time and sub-wavelength ultrafast coherent diffraction imaging in the extreme ultraviolet. Sci. Rep., 4: 7356.

**Return**

# IMPROVING THE TIME RESOLUTION OF THOMSON SCATTERING VIA MACHINE LEARNING ON REFLECTOMETRY DATA

D. R. Ferreira[1], A. Gillgren[2], A. Ludvig-Osipov[2], P. Strand[2] and JET Contributors[*]

[1]Instituto de Plasmas e Fusão Nuclear, Instituto Superior Técnico, Universidade de Lisboa, Portugal
[2]Department of Space, Earth and Environment, Chalmers University of Technology, Sweden
[*]See the author list of J. Mailloux et al 2022 Nucl. Fusion 62 042026
diogo.ferreira@tecnico.ulisboa.pt

**Abstract**

At the Joint European Torus (JET), the reference diagnostic to measure electron density is Thomson scattering. However, the low sampling rate of this diagnostic makes it impractical to study the dynamics of the density profile. In this work, we use machine learning to predict the density profile based on data from another diagnostic, namely reflectometry. The proposed model is trained to transform reflectometry data into Thomson scattering profiles, and is able to generate density profiles at a much higher sampling rate than Thomson scattering, and more accurately than reflectometry alone. This enables the study of pedestal dynamics and other edge phenomena.

## INTRODUCTION

High resolution Thomson scattering (HRTS) is the reference diagnostic for measuring the density profile at JET (Pasqualotto et al., 2004). This diagnostic provides good accuracy in terms of radial position (Frassinetti et al., 2012) but has a low sampling rate (20 Hz), which makes it infeasible to analyze pedestal dynamics in detail, namely phenomena such as edge localized modes (ELMs). These occur on faster time scales and would require a sampling rate on the order of at least 1 kHz to capture the transient processes associated with ELM crashes.

On the other hand, the reflectometry diagnostic at JET (Sirinelli et al., 2010) provides a high temporal resolution, and is able reconstruct the density profile at a sampling rate that is typically in the range of 1–10 kHz. However, this diagnostic is not as accurate in terms of the radial position of its density measurements, and over the years new and improved methods have been developed for the reconstruction of the density profile from reflectometry data (Morales et al., 2017).

The two diagnostics are based on different principles. Thomson scattering, which we will refer to as HRTS, is based on laser scattering, where density values are measured at fixed positions from the intensity of scattered light. On the other hand, the reflectometry diagnostic, which we will refer to as KG10 (its internal name at JET), is based on probing the plasma with electromagnetic waves over a wide range of frequencies (44–150 GHz). Each frequency value corresponds to a density value that is known beforehand, because that is the point where reflection occurs; however, the position of that point will have to be calculated from the travel time of the reflected wave.

In summary, HRTS measures density values at precise positions but with some uncertainty in those measurements, whereas KG10 measures precise density values but with some uncertainty in the positions of those measurements. Our goal is to take advantage of the high temporal resolution of reflectometry in order to derive Thomson scattering profiles at a much higher sampling rate than this diagnostic is able to provide. For this purpose, we use machine learning to train a neural network that maps KG10 to HRTS data. Once trained, the model can generate density profiles similar to HRTS at the sampling rate of KG10, even when HRTS is not available. This can be used, for example, to study pedestal dynamics in detail, as we illustrate in the sections below.

## MACHINE LEARNING APPROACH

Figure 1 shows two examples of how the two diagnostics may agree or disagree on the density profile. On the left-hand side, Figure 1 shows an example where both diagnostics are in good agreement: KG10 is able to probe the profile further inwards, but both diagnostics agree on the position of the pedestal, for example. On the right-hand side, Figure 1 shows an example where

there are miscalculations in the positions of the density values measured by KG10. When those errors occur, they tend to accumulate over subsequent positions, resulting in a density profile that does not match the one provided by HRTS. Fortunately, these problems occur in a small percentage of cases (~5%) and it would be desirable, if possible, to correct them via machine learning.

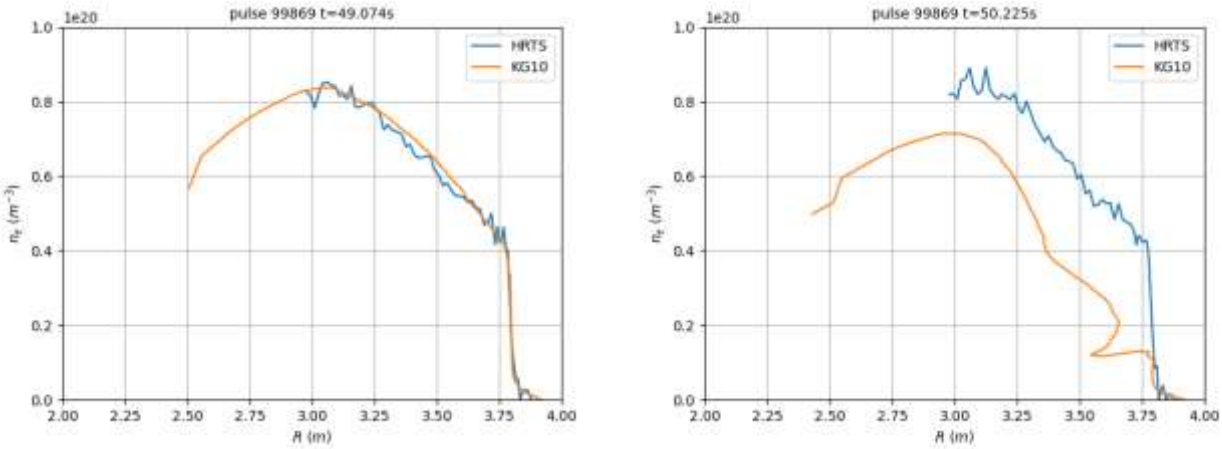


**Figure 1. Comparison of HRTS and KG10 profiles at two different times in the same pulse.**

To train a machine learning model to map KG10 to HRTS data, it is necessary to have instances where data from both diagnostics are available. In other words, we need training examples where both the HRTS and KG10 profiles are known. Since the sampling rate of KG10 is much higher than that of HRTS, in general for any given HRTS profile it is possible to find a KG10 profile that is close in time. The difference in time will be at most half the sampling period of KG10, which is on the order of $10^{-4}$ s. We refer to this process as the time-syncing of HRTS and KG10.

After the model is trained, it can be used to predict the HRTS profile when only the KG10 profile is known. This yields a virtual HRTS diagnostic with the sampling rate of KG10.

The model itself is a 4-layer neural network with a 100-dimensional input, which corresponds to the size of a KG10 profile, and a 63-dimensional output, which corresponds to the size of an HRTS profile. As shown in Figure 2, each dense layer has 1024 units, and it includes a ReLU (rectified linear unit) activation. The total number of parameters exceeds $3\times10^6$. The generous number of layers and parameters are motivated by the need to transform KG10 into HRTS data as accurately as possible, while overcoming the occasional issues with KG10 profiles. For this purpose, it turns out that having more layers, and hence more non-linearities, is more beneficial than having fewer and wider layers, and the model is also easier to train.

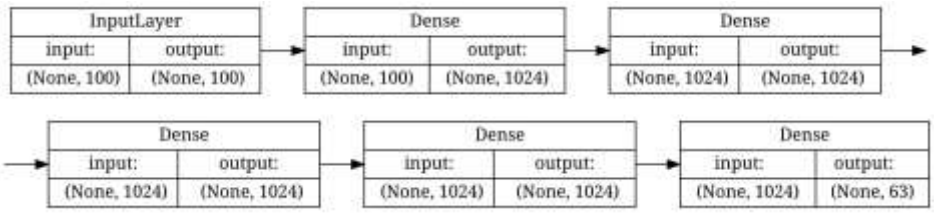


**Figure 2. Structure of the machine learning model.**

## TRAINING DATA

Before collecting the training data, we ensured that both diagnostics were fully operational for any experimental session that we selected for the training examples; this is the case from December 2020 onwards. In addition, the training examples should be representative of the type of experiments performed at JET; for this purpose, we selected experimental sessions from the baseline and hybrid scenarios (Garzotti et al., 2019). Specifically, we focused on the baseline and hybrid experiments performed in the C40 campaign (March–July 2021) and in the C41 campaign

(August–December 2021), which was the second Deuterium-Tritium campaign at JET (DTE2), after the first D-T campaign back in 1997.

From these experiments, we identified a total of 170 pulses, in the range of pulse numbers from 98794 to 99953. Since HRTS has a sampling rate of 20 Hz, and each pulse lasts for about 30 s, we expected a number of training examples on the order of $170 \times 30 \times 20 \approx 10^5$. In practice, we obtained 43 531 training examples of KG10–HRTS profile pairs. This was due to a number of reasons, including the fact that, while HRTS is operational during the entire pulse, KG10 has a shorter operating window because of limited data buffer capacity.

The training examples have been split into 90% for training and 10% for validation, and the model took 5 minutes to train on a single GPU (graphics processing unit). To analyze the variance of the results, we repeated the training procedure across a 10-fold cross validation.

## RESULTS

Figure 3 shows the predictions of the density profile for the same pulse and times that were illustrated before in Figure 1. Here, the red line is the mean prediction of the 10 models trained by cross validation, and the light-red band around it denotes the standard deviation. On the left-hand side in Figure 3, where KG10 and HRTS agree, the prediction also coincides with HRTS. The band around the prediction is hardly noticeable because all the models yield almost identical results. In the plot on the right-hand side, the model again provides a prediction that coincides with HRTS, despite the large gap that exists between the HRTS and KG10 profiles. We conclude that all those models can overcome the problems in the KG10 profile by providing predictions that are consistently close to the HRTS profile.

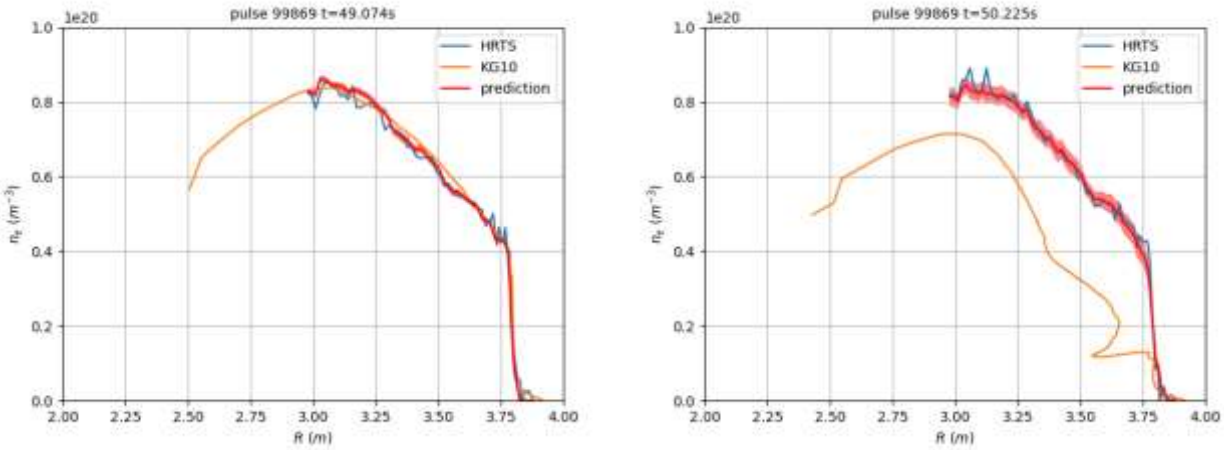


**Figure 3. Prediction of HRTS profile from KG10 data at two different times in the same pulse.**

The pulse that has been used to produce these results is in fact the record-breaking JET pulse of the Deuterium-Tritium campaign (DTE2). This pulse has not been used for training or validation, so the results in this section are meant to illustrate how the model performs on unseen data.

Our main goal, however, is to use the model to study the pedestal dynamics, particularly the processes at the time scale of an ELM cycle. Figure 4 illustrates two views over an ELM cycle at around t = 50.0 s in the same pulse. The density profile is predicted at the sampling rate of KG10, and is averaged over a sliding window of 1 ms. Figure 4 shows how the top of the pedestal (at around position R = 3.8 m) gradually builds up, until it crashes abruptly and a new build-up process is initiated. This particular ELM cycle lasts for about 30 ms, which is consistent with the range of 15–40 Hz for ELM frequencies at JET (Lennholm et al., 2015).

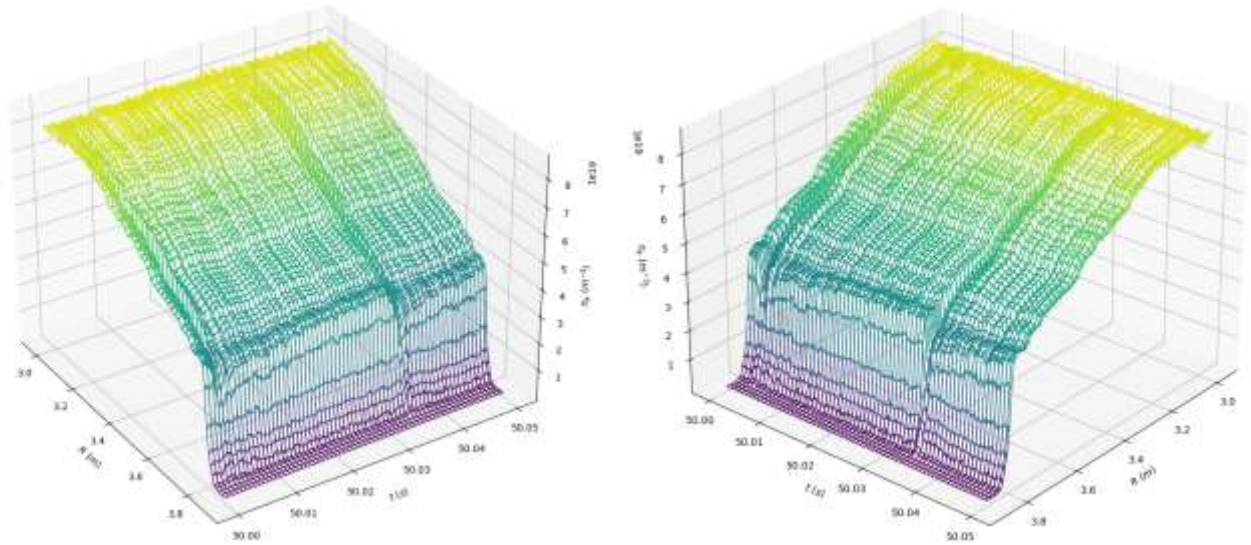

**Figure 4. Two views of the course of an ELM cycle at around t=50.0s in pulse 99869.**

## CONCLUSION

The proposed model predicts HRTS-like profiles from KG10 data assuming that HRTS provides the ground truth for the density profile, but it should be noted that HRTS itself is sometimes calibrated on KG10. Although our focus is on predicting the HRTS profile, we have not relegated KG10 to secondary importance; on the contrary, KG10 is essential to enable this approach, even with its occasional issues in position accuracy. These issues were mitigated by using a non-linear model with multiple layers and a large number of parameters. Still, the model is fast to train and use, and can be applied on any pulse with KG10 data, enabling the analysis of pedestal dynamics, ELMs, and other features of the density profile.

## REFERENCES


L. Frassinetti, M. N. A. Beurskens, R. Scannell, T. H. Osborne, J. Flanagan, M. Kempenaars, M. Maslov, R. Pasqualotto, M. Walsh and JET-EFDA Contributors (2012). Spatial resolution of the JET Thomson scattering system. Rev Sci Instrum 83: 013506.

R. Pasqualotto, P. Nielsen, C. Gowers, M. Beurskens, M. Kempenaars, T. Carlstrom, D. Johnson and JET-EFDA Contributors (2004). High resolution Thomson scattering for Joint European Torus (JET). Rev Sci Instrum 75: 3891–3893.

A. Sirinelli, B. Alper, C. Bottereau, F. Clairet, L. Cupido, J. Fessey, C. Hogben, L. Meneses, G. Sandford, M. J. Walsh and JET-EFDA Contributors (2010). Multiband reflectometry system for density profile measurement with high temporal resolution on JET tokamak. Rev Sci Instrum 81: 10D939.

R. B. Morales, S. Hacquin, S. Heuraux, R. Sabot (2017). New density profile reconstruction methods in X-mode reflectometry. Rev Sci Instrum 88: 043503.

L. Garzotti, C. Challis, R. Dumont, D. Frigione, J. Graves, E. Lerche, J. Mailloux, M. Mantsinen, F. Rimini, F. Casson, A. Czarnecka, J. Eriksson, R. Felton, L. Frassinetti, D. Gallart, J. Garcia, C. Giroud, E. Joffrin, Hyun-Tae Kim, N. Krawczyk, M. Lennholm, P. Lomas, C. Lowry, L. Meneses, I. Nunes, C.M. Roach, M. Romanelli, S. Sharapov, S. Silburn, A. Sips, E. Stefániková, M. Tsalas, D. Valcarcel, M. Valovič and JET Contributors (2019). Scenario development for D-T operation at JET. Nucl Fusion 59: 076037.

M. Lennholm, P.S. Beaumont, I.S. Carvalho, I.T. Chapman, R. Felton, D. Frigione, L. Garzotti, A. Goodyear, J. Graves, D. Grist, S. Jachmich, P. Lang, E. Lerche, E. de la Luna, R. Mooney, J. Morris, M.F.F. Nave, F. Rimini, G. Sips, E. Solano, M. Tsalas and JET EFDA Contributors (2015). ELM frequency feedback control on JET. Nucl Fusion 55: 063004


**Return**

# Status of the EUROfusion Enabling Research Project: *Advances in real-time reflectometry plasma tracking, for next generation machines*

F. da Silva[1], J. Santos[1], A. Silva[1], J. Ferreira[1], E. Ricardo[1], S. Heuraux[2], R. Sabot[3], F. Clairet[3], Y. Moudden[3], G. De Masi[4], R. Cavazzana[4], G. Marchiori[4], R. Bianchetti Morales[5], P. R. Resende[6], J. C. Abrantes[6], R. Luís[1], Y. Nietiadi[1]

[1]Instituto de Plasmas e Fusão Nuclear, Instituto Superior Técnico, Lisbon, Portugal
[2]Institut Jean Lamour, Université de Lorraine, CNRS, F-54000 Nancy, France
[3]IRFM - CEA Cadarache, Saint-Paul-lez-Durance Cedex, France
[4]Consorzio RFX C.so. Stati Uniti,4, 35127 Padova, Italy
[5]UK Atomic Energy Authority/Culham Centre for Fusion, Oxfordshire, United Kingdom
[6]proMetheus, Instituto Politécnico de Viana do Castelo, Viana do Castelo, Portugal
tanatos@ipfn.tecnico.ulisboa.pt

**Abstract**

We have put forward an Enabling Research Project (EnR) to contribute to the conceptualization of a reflectometry system able to provide control inputs not only in steady-state operation (flattop) but also during the initial stage of the discharge (ramp-up phase), paving the away to the use of plasma position reflectometry in next next-generation machines, such as DEMO. We propose an integrated approach involving different areas of research, such as the development of simulation codes and synthetic diagnostics, the development of new algorithms, synchronization between different reflectometer systems, and advances in reflectometry hardware, coming together coherently, in a forthcoming diagnostic. This paper shows the main issues addressed in this EnR and presents its status at the mid-term of the project.

## 7. MOTIVATION AND OBJECTIVES

One of the major roles for expected for reflectometry in DEMO will be plasma positioning and shaping control, complementing or effectively substituting magnetic diagnostics. The first steps to achieve this goal have already been taken experimentally, theoretically, and with simulations (Santos, 2012) but a great amount of groundwork remains to be done. An EUROfusion Enabling Research Project (ENR-TEC.01.IST) was built involving a team of experts and developers of reflectometry systems in Europe aiming to tackle many of the still remaining open questions and come out with a coherent and unified approach allowing to implement a reflectometry system able to provide control inputs not only in steady-state operation (flattop) but also during the initial stage of the discharge (ramp-up phase). The objectives and associated outcomes are divided into two main branches with their own specificities and requiring different approaches: (i) The ability to track and monitor the position and shape of the plasma in the start-up phase of the discharge and also at its ramp-down phase; (ii) To improve the capabilities of operation in the stationary phase (flattop) in order to provide an accurate and precise substitute to the positioning magnetic diagnostics in real-time. An important issue that must be addressed is the synchronization between all reflectometers. An experimental validation on the tokamak WEST will prove the concepts of synchronizing several reflectometers sharing the same clock and synchronizing triggering events. The project also contemplates advances in hardware with a prototype of a compact coherent fast frequency sweeping radio frequency (RF) back-end being developed using commercial Monolithic Microwave Integrated Circuits (MMIC) with Direct Digital Synthesis (DDS), which allows for full control of the signal's frequency and phase, both with very high precision and resolution.

## 8. THE EFFORTS DURING THE FIRST HALF OF THE PROJECT

DEMO's Plasma Position Reflectometry concept involves a set of poloidally distributed reflectometers (Marchiori, 2018). The final number of lines of sight (LOS) remains open and, at this point, the main restriction on the table are the waveguide accesses, which are limited and ultimately will determine how many antennas can face the plasma, see Figure 1-(a). Our proposal involves having the same hardware running with different modes of operation, see Figure 1-(b).

For the ramp-up, we propose an entirely new setup that will involve:

i. Interferometry.
ii. Refractometry.
iii. Intensity refractometry.

For steady state, the hardware will work as normal PPR reflectometers. Note that, in *D shaped* machines, little or no experience is available in using reflectometers for plasma density profile measurements outside the equatorial position.

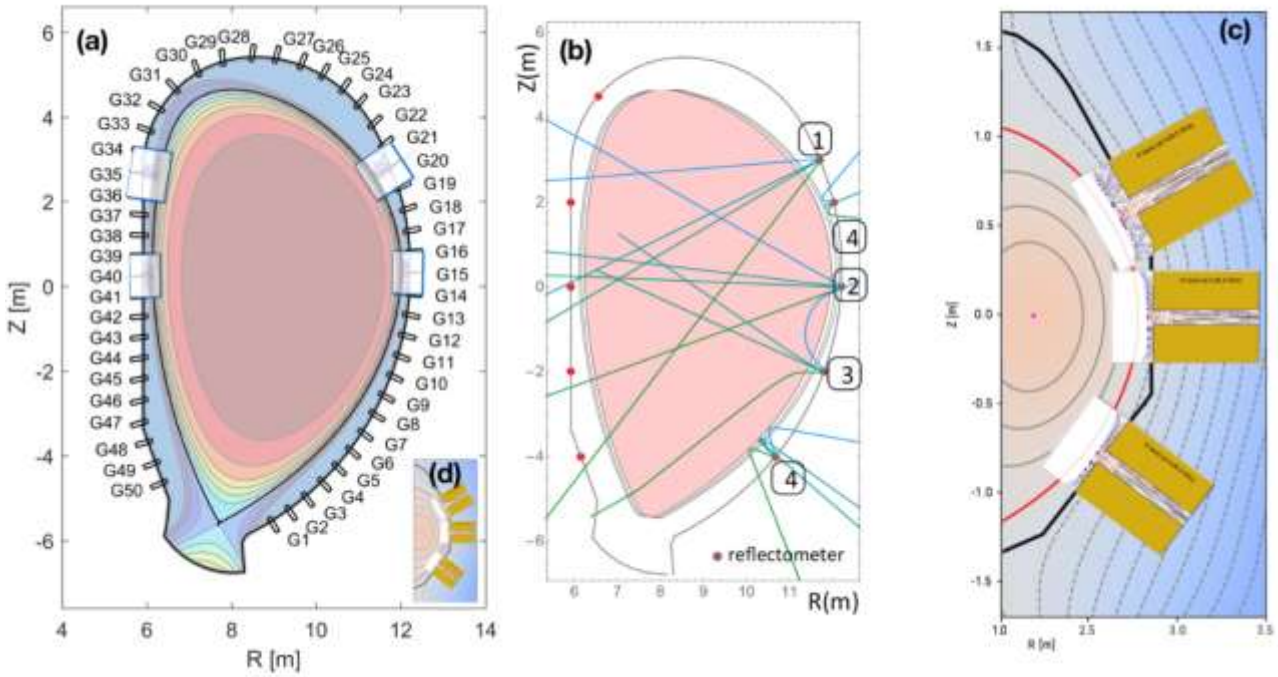


**Figure 1. (a) Concept of DEMO PPR involves several reflectometry LOS placed poloidally around the machine; (b) For ramp-up, a new diagnostic concept is being developed. The PPR hardware will work as an *interferometer* (1), as a *refractometer* (2) or as an *intensity refractometer* (3) as well as the standard *reflectometer* operation mode (4); (c) shows the LSF PPR synthetic diagnostics probing a DTT SN plasma; and (d) allows to compare the dimensions of the DTT vessel against DEMO's.**

These goals involve developments in different fields, namely (i) Development of synthetic diagnostics [prepare DEMO and DTT density inputs for simulation codes, developments in FDTD codes, developments in the description of structures (antennas/waveguides/vessel walls)], developments in the description of plasma scenarios); (ii) Development of new algorithms (for steady state and ramp-up); (iii) Synchronization between different reflectometers (experimental validation on the tokamak WEST); (iv) Advances on reflectometry hardware (compact reflectometer prototype using MMIC with DDS signal generation); and (v) DTT as a possible testbed for DEMO (Synthetic diagnostics for simulation and algorithms, design of antennas for a possible PPR implementation).

At the beginning of the EnR, the code REFMUL3 entered the production stage and was added to

the EnR codes' toolkit, making 3D simulations available. REFMUL3 is a 3D parallel code with all field components included. It has a parallel hybrid implementation (OpenMP+MPI) with 3D domain decomposition, showing very good scaling behavior, and a XDMF/HDF5 compressed binary output (da Silva 2022). Within the EnR ameliorations have been added, a pitstop/restart file implementation, a VTK format output, and an ancillary CAD import pipeline, allowing an unprecedented description of the synthetic diagnostics (Santos, 2021).

DEMO steady state has been comprehensively studied in this first half on the enabling research and with advances made in algorithms for steady state (Ricardo, 2021). We will devote the reminder of the project to research solutions pertinent to the ramp-up concept, namely with the identification of the many operational cases possible and which operational model to use associated with the appropriated interpretative model.

On the hardware development front, two compact reflectometer prototype PCB boards were developed and built using MMIC with a back-end covering directly 10 to 20 GHz, which with full band frequency multipliers can be extended to 140 GHz. The initial tests performed with these prototypes were very encouraging with the back-end prototype generating full band signals exceeding 8 dBm, enough to drive external multipliers. All undesirable harmonics are 15 dBi below the desired output, in all frequency ranges (Silva, 2021). Testing the quadrature detector will follow. An important feature to be implemented is DDS signal generation.

Concerning Synchronization between different reflectometers, the experimental validation on the tokamak WEST started with successful laboratory tests. However, the tests in situ in real environmental conditions have been postponed due to the delay of the WEST experimental campaign.

Works on DTT have progressed well with a comprehensive assessment of a LFS PPR system made with 2D simulations done with REFMULF code, see Figure 1-(c), complemented with 3D ones, performed with REFMUL3. During the project, the possibility of having a PPR system installed at DTT became tangible with the hypothesis of one or two LOS in the High Field Side (HFS). The concept of this tentative HFS system is needed as soon as possible since its deployment includes the installation of the waveguide access embedded in the structure of the vessel. This shifted our efforts from the LFS to the HFS, in particular to the design of the antennas and their integration in the first wall. The space available is at a premium and had to be taken into consideration. Two types of antennas are being proposed, the first for a bistatic system, and the second for a monostatic one.

## 9. STATUS OF THE WORK AT MID-TERM (27 SEPTEMBER 2022)

The status of the EnR Project at its midpoint is very encouraging with the vast majority of tasks either on schedule or completed, many of these with objectives surpassed. Further knowing that some of these tasks were not in the initial project proposal, but were rather late additions, one can vow for the good progress of the work. This can be confirmed in the following task accomplishment summary:

- Development of synthetic diagnostics
  - *DEMO and DTT density inputs for simulation codes - On schedule*
  - *Developments in FDTD codes (+REMUL3) - Completed (surpassed objectives)*
  - *Developments in the description of structures - Completed (surpassed objectives)*
  - *Developments in the description of plasma scenarios - Completed (surpassed objectives)*
- Development of new algorithms
  - *For steady-state - Completed*
  - *For ramp-up - On schedule with work intensifying in the remainder of EnR*
- Synchronization between different reflectometers
  - *An experimental validation on the tokamak WEST - Delayed*
- Advances in reflectometry hardware
  - *Compact reflectometer prototype using MMIC with DDS signal generation - On schedule*

- DTT as a possible testbed for DEMO
  - *Synthetic diagnostics for simulation and algorithms - On schedule*
  - *Design of antennas for a possible PPR implementation - On schedule*

So far, the EnR has produced some scientific output, two peer-reviewed publications and six communications to conferences and workshops. More publications are expected by the end of the project.

## 10. RECENT WORK SINCE MID-TERM

Since these mid-term milestones work has progressed, namely the status of the experimental validation synchronisation of WEST reflectometers has picked up its pace, with the implementation and test of the trigger synchronisation for the C8 campaign (starting in October). Also, outside the synchronisation work, but still in the scope of the ENR project, some hardware developments for real-time reflectometry measurements on WEST have been achieved. It is planned for a Ph.D. student to start his work, closely linked to the EnR project objectives, under the supervision of one of its members, Y. Moudden.

In the sequence of Request to Advanced Computing Hubs support, REFMUL3 is being adapted to run on GPU HPCs using OpenMP offloading with promising preliminary results.

For DTT, the CAD wall embedding of the newly designed HFS antennas and its conversion to REFMUL3 input format is afoot with the first simulation results for the bistatic antenna design in vacuum finished. Also, a 3D-printed mock-up bistatic antenna was done and the laboratory tests are underway.

First full-wave support simulations, for validation of ray trace studies of ramp-up, have started and will intensify in the last run of the EnR project.

## 11. ACKNOWLEDGMENT

This work has been carried out within the framework of the EUROfusion Consortium, funded by the European Union via the Euratom Research and Training Programme (Grant Agreement No 101052200—EUROfusion). The work has been carried out under the EUROfusion Enabling Research project ENR-TEC.01.IST. Views and opinions expressed are however those of the author(s) only and do not necessarily reflect those of the European Union or the European Commission. Neither the European Union nor the European Commission can be held responsible for them. IST activities also received financial support from Fundação para a Ciência e Tecnologia (FCT).

## 12. REFERENCES

da Silva, F., Ricardo, E., Ferreira, J., Santos, J., Heuraux, S., Silva, A., et al. (2022). Benchmarking 2D against 3D FDTD codes for the assessment of the measurement performance of a low field side plasma position reflectometer applicable to IDTT. Journal of Instrumentation, 17(01), C01017. http://doi.org/10.1088/1748-0221/17/01/C01017.

Marchiori, G. *et al*. (2018). Study of a Plasma Boundary Reconstruction Method Based on Reflectometric Measurements for Control Purposes. *IEEE Transactions on Plasma Science*, vol. 46(5):1285-1290, http://doi.org/10.1109/TPS.2018.2797549.

Ricardo, E. A. (2021), Assessment of reflectometry diagnostics for DEMO, Doctaoral Thesis, Instituto Superior Tecnico, Universidade Tecnica de Lisboa.

Santos, J., Guimarãis, L., Zilker, M., Treutterer, W., Manso, M. and the ASDEX Upgrade Team (2012), Reflectometry-based plasma position feedback control demonstration at ASDEX Upgrade, Nuclear Fusion, 52:032003. http://doi.org/10.1088/0029-5515/52/3/032003.

Santos, J. M., Ricardo, E., da Silva, F. J., Ribeiro, T., Heuraux, S., and Silva, A. (2021). A 3D CAD model input pipeline for REFMUL3 full-wave FDTD 3D simulator. Journal of Instrumentation, 16(11), C11013. http://doi.org/10.1088/1748-0221/16/11/C11013.

Silva, A. et al (2021), FM-CW compact reflectometer using DDS signal generation, Journal of Instrumentation 16:C11005. https://dx.doi.org/10.1088/1748-0221/16/11/C11005.

**Return**

# CONCEPTUAL DESIGN OF VISIBLE SPECTROSCOPY DIAGNOSTICS FOR DTT

A. Belpane[1,2], L. Carraro[1,3], A. Fassina[5], M. Cavedon[4], L. Senni[5]

1. Consorzio RFX (CNR, ENEA, INFN, Università di Padova, Acciaierie Venete SpA), Corso Stati Uniti 4, 35127 Padova, Italy
2. Department of Economics, Engineering, Society and Business Organization, University of Tuscia, Largo dell'Università, 01100 Viterbo, Italy;
3. CNR-ISTP Padova, Italy
4. Dipartimento di Fisica "G. Occhialini", Università di Milano-Bicocca, 20126 Milano, Italy
5. ENEA, Fusion and Nuclear Safety Department, 00044 Frascati, Italy

Email (andrea.belpane@igi.cnr.it)

## ABSTRACT

The project of the diagnostics for the $Z_{eff}$ radial profile measurement and for the divertor visible imaging spectroscopy, designed for the new tokamak DDT (Divertor Tokamak Test), is presented. To deal with the geometrical and functional constrains of DTT and to minimize the diagnostics volume inside the access pipe, an integrated and compact solution hosting the two systems has been proposed. The $Z_{eff}$ radial profile will be evaluated from the Bremsstrahlung radiation measurement in the visible spectral range, acquiring light along ten Lines of Sight (LoS) in the upper part of the poloidal plan. The plasma emission will be focused on optical fibers, which will carry it to the spectroscopy laboratory. A second equipment, with a single toroidal LoS crossing the plasma center and laying on the equatorial plane, will measure the average $Z_{eff}$ on a longer path. The divertor imaging system is designed to measure impurity and main gas influxes, to monitor the plasma position and kinetics of impurities, and to follow the plasma detachment evolution. The project aims at obtaining the maximum coverage of the divertor region. The collected light can be shared among different spectrometers and interferential filter devices placed outside the torus hall to easily change their setup. The system is composed of two endoscopes, an upper and a lower one, allowing a more perpendicular and a more tangential view of the divertor.

## 1. INTRODUCTION

In the roadmap of the European program toward nuclear fusion (EuroFusion, 2018), one of the most critical challenges is to design an adequate power exhaust solution that can work in the harsh environment of the Demonstration Fusion Power Plant (DEMO). In this context, the new Italian project DTT (Divertor Tokamak Test) (Ambrosino, 2021), which will be built at ENEA Frascati research center, near Rome, is meant to investigate alternative divertor solutions to optimize the configuration for DEMO. To fulfill this scientific goal the device will be equipped with a set of diagnostics specifically dedicated to the study of the edge and divertor regions, focusing on impurity level, thermal characterization, plasma detachment, degree of enrichment of impurities, level of helium compression and power exhaust (Albanese,2017). With these goals, during the first plasma operation, DTT will be equipped with a first group of machine and plasma diagnostics, the so-called DAY0 systems (Polli, 2022), of which the diagnostics presented in this work are part.

To deal with the geometrical and functional constrains of DTT (cryostat presence) and to minimize the diagnostics volume inside the access pipe, an integrated and compact solution hosting four spectroscopy systems has been proposed:

- A multi-chords diagnostic to evaluate $Z_{eff}$ profiles on the poloidal plane fortified with a robust measurement of the average $Z_{eff}$ along a toroidal LoS (Line of Sight)
- two imaging spectroscopy diagnostics aiming at measuring the impurity and main gas influx from the divertor plasma facing components (PFC), and at spectroscopically investigating the divertor region to monitor detachment phenomena.

## 2. EFFECTIVE CHARGE RADIAL PROFILE

The first system is a multi-chords diagnostic consisting of 11 telescopes that collect the emission from the plasma and then relay it through fibers to a laboratory room adjacent the Torus Hall. The system is subdivided in two sub-systems: 10 telescopes on the poloidal plane (see Figure 5.a) and the 11th with a toroidal view on the equatorial plane shown in Figure 5.b. Both subsystems use interferential filters centered at 523,5 nm ± 0,5 nm**,** a line-free spectral region to measure the Bremsstrahlung continuum. Main gas and impurity influxes could also be measured, with this system, adding filters and splitting the light directly in the laboratory.

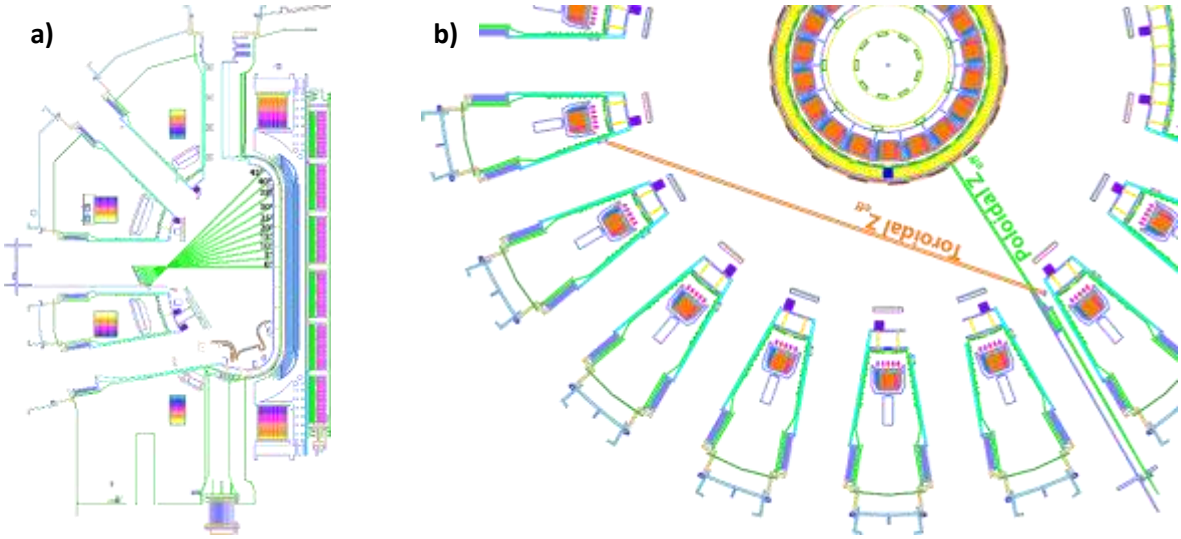


a **Figure 5 - Effective charge lines of sigh: a) tens lines of sight on the poloidal plane in the upper part of the vacuum vessel; b) toroidal line of sight on the equatorial plane**

Figure 5.a shows the 10 LoS that cover the upper part of the poloidal plane thus avoiding the strong radiation from the divertor region, which can contaminate the Bremsstrahlung spectrum. Dumps will be inserted where the $Z_{eff}$ LoS hits the internal first wall (on the high field side) in order to minimize reflection. The second $Z_{eff}$ subsystem is made up of a single telescope that acquires emission along a single line of sight on the equatorial plane (orange line in Figure 5). This toroidal LoS, crossing the plasma core for a longer path, allows to minimize contamination by the plasma edge emission, providing a more robust evaluation of the plasma core $Z_{eff}$. As for the poloidal $Z_{eff}$, the reflections are minimized by pointing the LoS inside a port.

The harsh environment prevents the usage of a window close to the plasma; therefore, a mirror-based system to bring the emission outside the vessel to the telescopes located nearby the cryostat has been designed, as can be seen in Figure 6. The mirrors have a clearance optical diameter allowing the alignment of the optical system through the telescopes' movement.

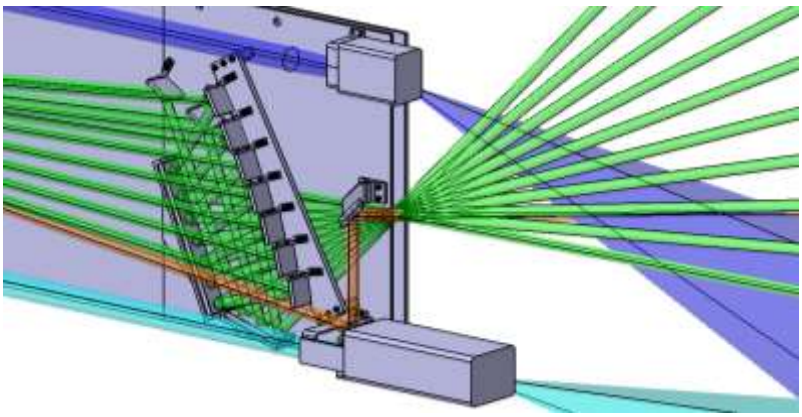

b **Figure 6 - Overview of the diagnostic**

## 3. DIVERTOR IMAGING SPECTROSCOPY

This sub-system aims at measuring the impurity and main gas influx from the plasma facing components (PFC), at spectroscopically investigating the divertor region, and at monitoring the detachment. The system is composed of two endoscopes that drive the emission outside the torus. The upper view, as reported in Figure 7.b, observes the divertor from a sloped view to see the divertor throats, (dark blue beam in Figure 6 and Figure 7) whereas the second one (light blue beam)), indicated as a lower view, has a more tangential, but wider vertical view for monitoring the detachment front movement. The spectral region of interest is 350-800 nm in order to monitor the ionization front movement and detachment onset, evolution and settlement.

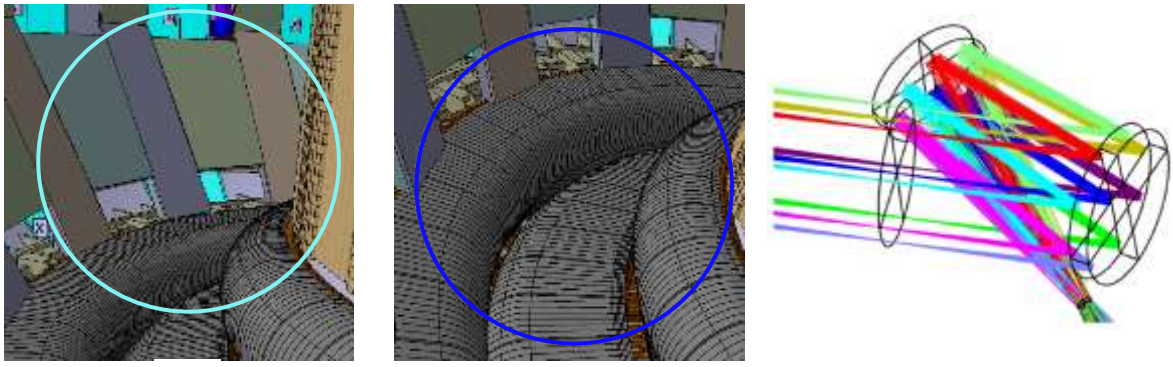

a) b) c)

c **Figure 7 - a) tangential view of the divertor region; b) vertical view of the divetor; c) ray tracing simulation of the mirror installed inside the optical head**

In Figure 6 it can be seen that both systems are composed by similar structures (blue and light blue beams). Both heads are made of a metallic box that protects the optical elements: two mirrors, M1 flat, M2 parabolic (f=1993mm; k=-1) with an optical diameter of 50 mm allowing a spatial resolution of ~ 1 cm. The heads will host a shutter system, to protect the mirrors during wall conditioning operations, which will be equipped with a cooling system to cope with the intense thermal loads from the plasma.

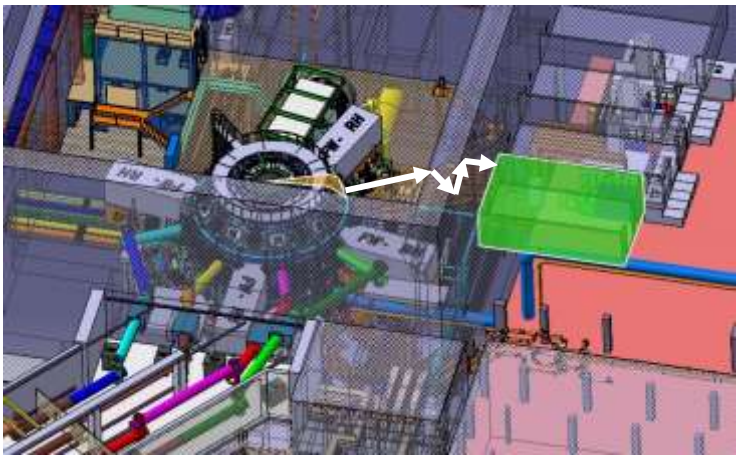

**Figure 8 - Ray path from the torus to the laboratory**

The possibility of placing the spectroscopic instruments operating in the visible range outside the torus hall will be pursued, in order to share light among different spectrometers and interferential filter devices and to allow easy access to the instruments' setup. To pursue this goal the emission from the torus must be relayed to the laboratory, along a path about 25 m long. To avoid chromatic aberrations a mirror-based relay system is being designed.

## 4. CONCLUSION AND FUTURE WORK

In this work, the conceptual design of the main visible spectroscopy diagnostic systems for DTT was presented. A solution that ensures the performance target of different spectroscopy systems and, at the same time, fits the geometrical constrains of the device port has been found. The space and the form adopted take into account the harsh environment, in which the system will work. The next steps to finalize the diagnostic include the support components that must be installed in the torus hall, the design of the cooling system and of the mirror-based relay system to bring the divertor image from the vessel to the laboratory.

## 5. REFERENCES

EuroFusion. (2018) "*European Research Roadmap to the Realization of Fusion Energy*".URL: https://euro-fusion.org/eurofusion/roadmap/

R. Albanese, et al. (2017) "*Diagnostics, data acquisition and control of the divertor test tokamak experiment*". In: Fusion Engineering and Design 122. DOI: http://dx.doi.org/10.1016/j.fusengdes.2017.05.118

R. Ambrosino, et al. (2021) "*DTT - Divertor Tokamak Test facility: A testbed for DEMO*". In: Fusion Engineering and Design 167. DOI: https://doi.org/10.1016/j.fusengdes.2021.112330

G. M. Polli, et al. (2022) "*Status of design and procurement activities in DTT tokamak project area*". In: IEEE 21st Mediterranean Electrotechnical Conference 477-482. DOI: 10.1109/MELECON53508.2022.9843123

**Return**

# REAL-TIME ELECTRON TEMPERATURE AND DENSITY MEASUREMENT BY THOMSON SCATTERING FOR PLASMA CONTROL ON LHD

Funaba, H[1], Yamada, I[1], Yasuhara, R[1], Kenmochi, N[1], Morishita, Y[2], Murakami, S[2], Lee, J-H[3], Nakanishi, H[1], Osakabe, M[1]

[1]National Institute for Fusion Science, National Institutes of Natural Sciences, Toki, Gifu 509-5292, Japan
[2]Department of Nuclear Engineering, Kyoto University, Nishikyo, Kyoto, 615-8540, Japan
[3]Korea Institute of Fusion Energy, Daejeon 34133, Korea
funaba.hisamichi@nifs.ac.jp

**Abstract**

- Real-time measurement of the spatial profiles of the electron temperature and density is required for the Thomson scattering system on the Large Helical Device. The real-time data processing is made by the new fast digitizers and the RTRetrieve data acquisition system. Although the calculation time of the electron temperature and density is almost 18 ms, the total delay time from the laser pulse to the output of the results is up to 100 ms. This delay time is enough for the ASTI system, which is a data assimilation system for integrated transport simulation of fusion plasma.

## 1. INTRODUCTION

Ral-time information of the electron temperature, $T_e$, and the electron density, $n_e$, profiles can be used for evaluating or controlling the heating profiles, the magnetic configurations, the divertor detachment, and so on (Laggner, et al., 2019, Eldon, et al., 2017). For example, in the real-time Thomson scattering system on KSTAR (Lee S-J, et al., 2020, Lee S-J, et al., 2021, Lee J-H, et al., 2023), $T_e$ data are provided for the PCS (Plasma Control System). The GPU system is used for the data processing with Fourier transform and $T_e$ calculation by the neural network. Figure 1 shows a schematic diagram of a real-time measurement by the Thomson scattering system. The scattered light from the plasma is dispersed by the polychromators and the signals are acquired by the fast digitizers. The data are transferred from the acquisition PC to the data analysis PC just after the acquisition of the signals. The calculation of $T_e$ and $n_e$ are made in real-time on the analysis PC.

The real-time measurement of the spatial profiles of $T_e$, and $n_e$ is required for the Thomson scattering diagnostics on the Large Helical Device (LHD) (Narihara, et al., 2001, Yamada, et al., 2010) by the ASTI system (Assimilation System for Toroidal plasma Integrated simulation), which is developed in Kyoto University (Morishita, et al., 2022). The experiments of the plasma control by ASTI started on LHD in 2022. It is considered that the following controls become possible by the ASTI system: (1) Real-time plasma control with the data from multiple diagnostics, (2) Prediction of some phenomena (e.g., radiation collapse etc.) with the modeling of them.

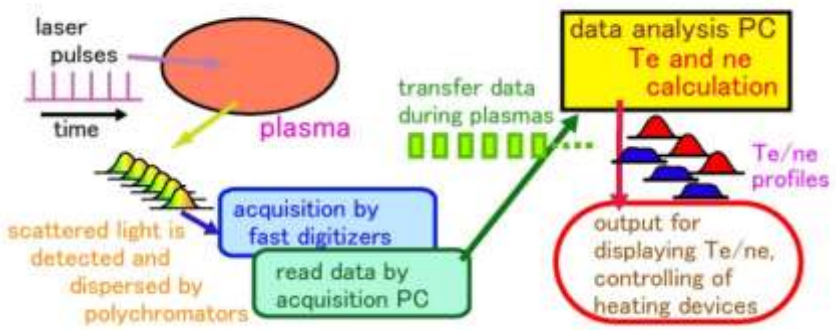


**Figure 1. A schematic diagram of a real-time measurement by the Thomson scattering system.**

In this study, it is intended to read the Thomson scattering signals and to calculate $T_e$ and $n_e$ in a few tens of milliseconds during plasma discharges in order to predict and control the temporal development of the plasma parameters, such as $T_e$ and $n_e$, through the transport simulation by the ASTI system. The data processing and calculation time are recorded in detail and adjusted for the real-time measurement.

Section 2 describes the systems for the real-time data acquisition and the analysis system. The results of the real-time measurement are shown in Sec. 3. Section 4 is a conclusion.

## 2. MATERIALS AND METHODS

Although the LHD Thomson scattering system has 144 spatial points for measurement, signals from 70 points are used for the real-time measurement. Fast digitizers of the switched-capacitor type (TechnoAP APV85G32L), which obtain the fast signals with their time development, are used. These digitizers are installed for the Thomson scattering measurement with a high repetition rate laser of 20 kHz (Funaba, et al., 2022).

The data transmission process is shown in Fig. 2. The data are read by the analysis program through the RTRetrieve system (Nakanishi, et al., 2016). The data transferring starts by the command "RTCtransfer" and the data are stored in the memory of the analysis PC. The reading program reads the one channel data by the "RTCgetChannelData" command. The number of the data for one laser pulse is 32 channels times 12 digitizer boards. The usual, not dedicated, network is used for the data transfer between the acquisition PC and the analysis PC.

In the data analysis PC, the signals are integrated in time and $T_e$ is calculated by the $\chi^2$-method. $n_e$ is derivid with the calibration resulats of Raman scatterig.

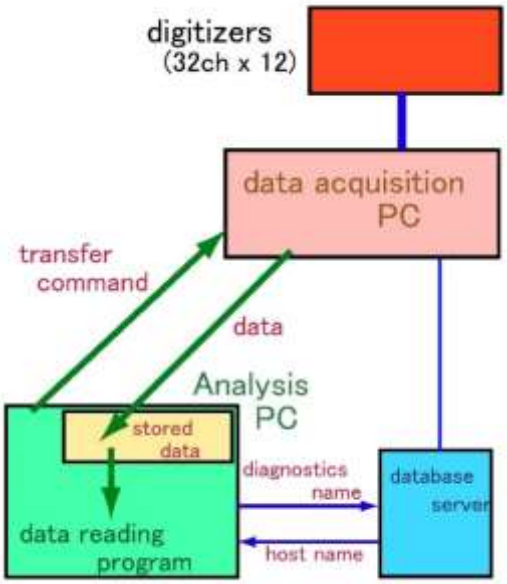


**A.** **Figure 2. Real-time data acquisition by the RTRetrieve system (Nakanishi, et al., 2016) on LHD.**

**B.**

As shown in Fig. 3, the $T_e$ and $n_e$ profiles are transmitted to a vector engine server SX-Aurora TSUBASA in real-time by the socket communication and used as inputs of the ASTI system. The output of the ASTI system is used for the control of the plasmas by the heating devices. The control of the electron cyclotron heating (ECH) system is connected to this system at present. Since the ASTI system read the data in 10 Hz, the required delay time is within 100 ms at present. The input and output which are shown in the broken boxes in Fig. 2 are under planning and not installed.

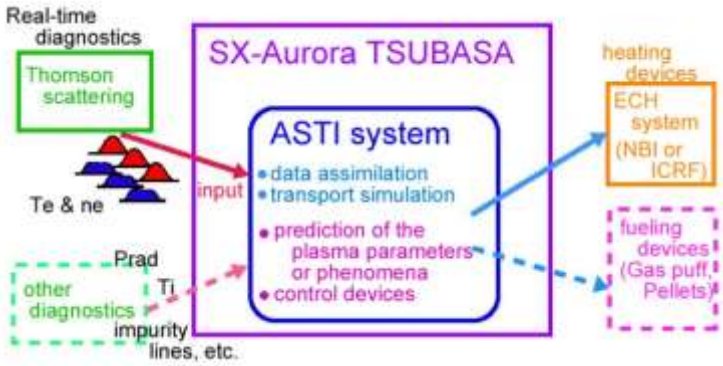


C. **Figure 3. A schematic diagram of inputs and outputs in the ASTI system.**

D. **Inside the broken boxes are under planning.**

## 3. RESULTS AND DISCUSSION

The real-time measurement by the Thomson scattering diagnostics was operated in the 10 Hz of the repetition frequency. Figure 4 shows an example of the real-time monitoring of the $T_e$ and $n_e$ profiles at $t$ = 3.60 s. This picture was taken from a movie in which the real-time measurement during the LHD plasma of #183873 was recorded. The red and blue data show the $T_e$ profile and the $n_e$ profile, respectively. The camera images of the plasma at the same time are shown in the multi-screen display in the right side.

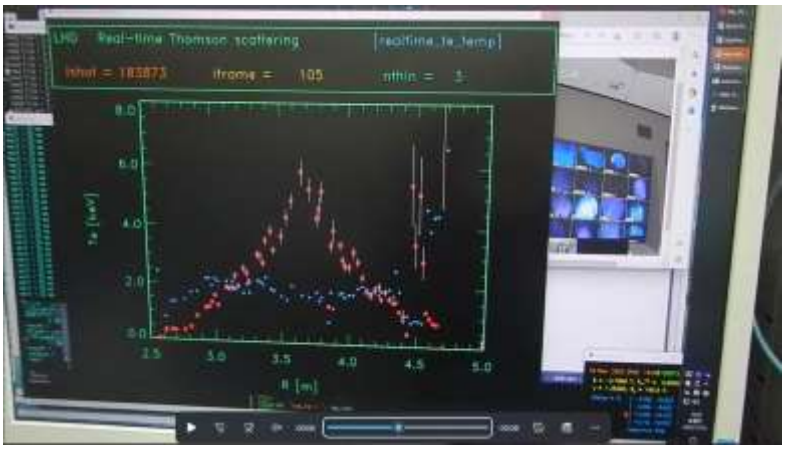

**Figure 4. An Example of the real-time monitoring of the $T_e$ and $n_e$ profiles by the Thomson scattering diagnostics.**

In order to evaluate the delay time from the laser pulse, $t_{delay}$, it is divided in three as follows.

$$t_{delay} = t_{d1} + t_{d2} + t_{d3} \quad [1]$$

$t_{d1}$ : Time between the laser pulse and reading of all data in the data analysis PC
$t_{d2}$ : Calculation time in the data analysis PC
$t_{d3}$ : Data transmission time between the data analysis PC and the plasma control system

The detailed timings of the calculation are recorded in a log-file as shown in Fig. 5. Timings are written at some of the red lines. The time from the start timing of the sequence ($t$ = 0 s) and the time from the previous output are shon by "from start" and "passed" in these lines, respectively. The calculation time for $T_e$ and $n_e$ are 12 ms and 6 ms, respectively. Therefore, $t_{d2}$ is 18 ms in this case. At the blue line, the process for the signals by the laser pulse at $t$ = 5.7 s started. The first data are read after 33 ms. Almost all of the data are read within 1 ms since the data are stored in the memory of the analysis PC. However, waiting times of 15 - 33 ms are needed before reading a few signals of

the data. The total reding time $t_{d1}$ becomes about 70 ms. However, no accumulation of the delay time was observed.

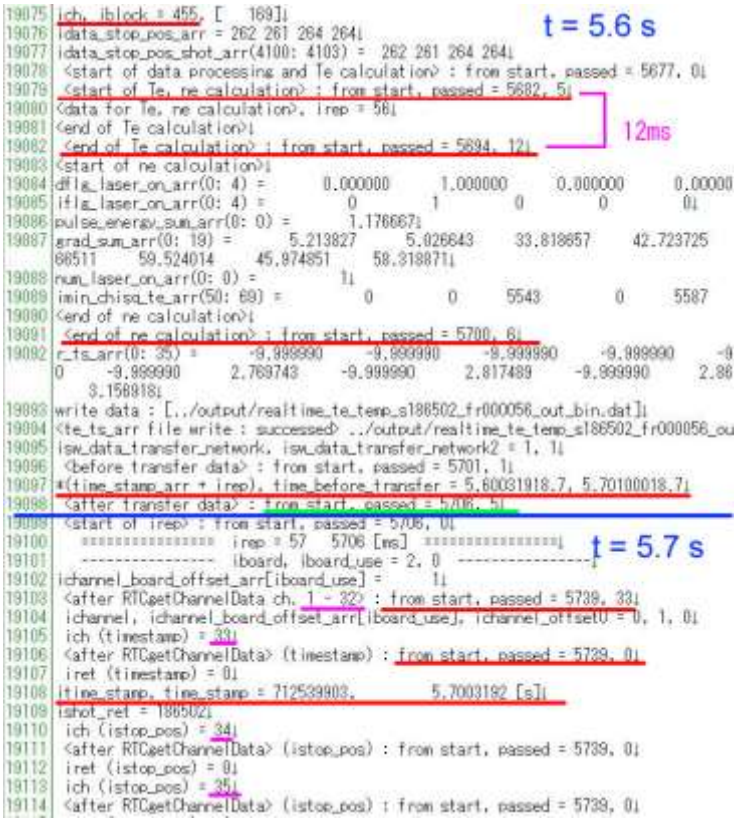


**Figure 5. Texts from a log file of the real-time measurement program around t = 5.7 s.**

## 4. CONCLUSION

The real-time Thomson scattering system started to operate and provide $T_e$ and $n_e$ profiles to the ASTI system with the repetition rate of 10 Hz and the delay time up to 100 ms. The delay time within 100 ms is enough for the ASTI operation at present. No accumulation of the delay time was found. The details of the delay time were evaluated. The data reading time is almost 70 ms and the calculation time is about 18 ms. The value of the data reading time seems to be long. In order to reduce this time, the multithreading will be applied for data reading by the RTRetrieve system.

## ACKNOWLEDGMENT

The authors appreciate the assistance of the LABCOM group in NIFS. This work is supported partially by NIFS20ULHH005, NIFS22KIPT008, JSPS KAKENHI Grant Numbers 15KK02451, 21K13901 and 23H01162. This work is in cooperation with KFE-EN2101-12 with Ministry of Science and ICT under KFE R&D Program.

## REFERENCES

Eldon, D, *et al.*, (2017) Nucl. Fusion 57: 066039.
Funaba, H, *et al.*, (2022) Sci. Rep. 12: 15112.
Laggner FM, *et al.*, (2019) Rev. Sci. Instrum. 90: 043501.
Lee, S-J, *et al.*, (2020) Fusion Eng. Des. 158: 111624.
Lee, S-J, *et al.*, (2021) Fusion Eng. Des. 171: 112546.
Lee, J-H, *et al.*, (2023) Fusion Eng. Des. 190: 113532.
Morishita, Y, *et al.*, (2022) Comput. Phys. Commun. 274: 108287 .
Nakanishi, H, *et al.*, (2016) IEEE Trans. Nucl. Sci. 63: 222.
Narihara, K, *et al.*, (2001) Rev. Sci. Instrum. 72: 1122.
Yamada, I, *et al.*, (2010) Fusion Sci. Tech. 58: 345.

**Return**

# CVD Diamond Tomography for the DTT Fusion Device

Bombarda, F.[1], Palomba, S.[2], Cesaroni, S.[1], Verona, C.[2], Verona-Rinati, G.[2], Marinelli, M.[2], Angelone, M.[1], Iafrati, M.[1]

[1] ENEA, Fusion and Nuclear Safety Department, Frascati (Rome), Italy

[2] "Tor Vergata" University of Rome, Industrial Engineering Department, Rome, Italy

silvia.palomba@uniroma2.it

**Abstract**

The conceptual design of the tomography system for DTT is advancing on both the selection of the detectors' characteristics and on the reconstruction of phantom emission profiles to determine the best combination of the detectors number and position. Single crystal CVD diamonds are likely the most viable choice to place in close proximity of the plasma for UV and SX detection. The new configuration of CVD detector for lateral irradiation (LAT) was designed for a more efficient detection of photons up to 30 keV, while the standard layered configuration is sensitive to energies as low as 5.5 eV up to 2-3 keV. A pixel-based code was developed that utilizes the minimization of $\chi^2$ with the Tikhonov regularization matrix. The simulations carried out so far indicate that about 96 diodes suitably distributed on the four available ports of the machine are an adequate number for proper reconstruction of simple gaussian phantoms, provided good coverage of the outer edge region is ensured.

## 1. INTRODUCTION

The DTT tokamak (Ambrosino et al., 2021), presently under construction at Frascati (Rome, Italy), is a relatively large device of major radius $R$ = 2.19 m, minor radius $a$ = 0.70 m, toroidal field on axis $B_T$ = 6 T, plasma current $I_p$ = 5.5 MA. The pulse length is expected to reach 100 s, with plasma density and temperature of $1.8\times10^{20}$ m$^{-3}$ and 6.1 keV respectively, when heated by 45 MW of additional power. Even if designed to operate with Deuterium fuel, the neutron and gamma radiation fluxes will pose substantial challenges for any diagnostic system required to operate in the proximity of, or inside the vacuum vessel. In such harsh environment, the suitability of Si or CdTe diodes for full plasma tomography is not obvious and requires careful assessment.

For this reason, and also to extend the accessible spectral range, the use of a different kind of UV-SX photon detectors diodes is proposed, namely the thin single crystal, Chemical Vapor Deposition (CVD) diamond detectors being produced at the laboratory of Industrial Engineering Department of the University of "Tor Vergata" in Rome. These have been successfully tested on JET (Angelone et al., 2010) and FTU (Bombarda et al., 2021), but never in full tomographic layout (in fact only two detectors were installed on each machine), and their locations were so removed from the torus that both radiation and heat could not be of concern. Even with just single line-of-sights, they proved capable of providing valuable information of the plasma behavior and its dynamics.

## 2. CHARACTERISTICS OF CVD DIAMOND PHOTODETECTORS

The CVD diamonds exhibit a number of attractive features: they are sensitive to radiation from

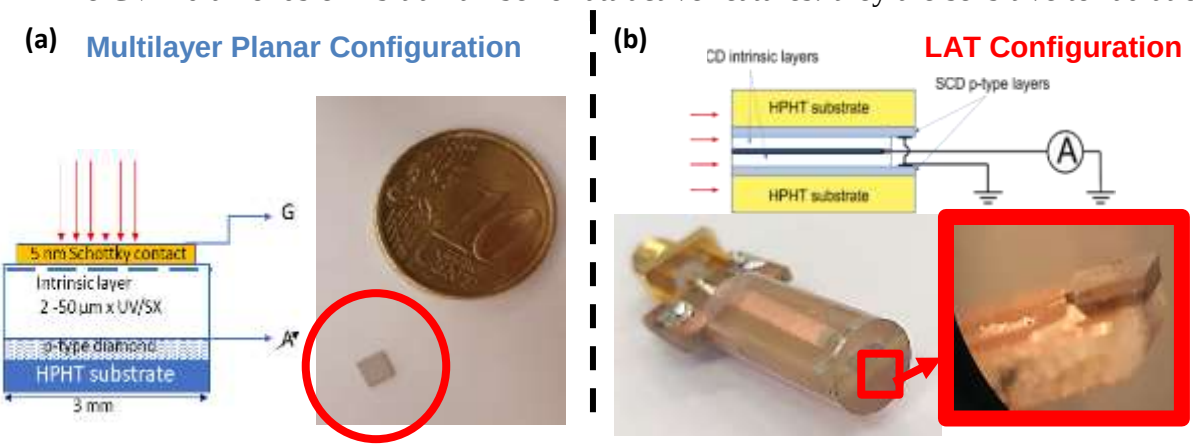


**Figure 9 (a) The Multilayer Planar configuration used at JET and FTU, suitable for photon energy < 5 keV; (b) the new LAT configuration to be used for photon energies up to 30 keV impinging on the side.**

5.5 eV up to tens of keV but are visible blind; the wide band gap ensures low leakage currents; they are much more radiation resistant than silicon, especially the thin samples suitable for photon detection. Irradiation tests carried out at the Frascati Neutron Generator up to fluences of $2\times10^{18}$ of 14 MeV n/m$^2$ showed no appreciable degradation (Pillon et al., 2008). They can operate at room temperature with very high S/N ratios, are very small in size and, most importantly, they can be placed in the machine high vacuum, without need for Be windows. Furthermore, considering the geometry of DTT port ducts, the coverage of the plasma poloidal section required for a proper tomographic inversion is possible only by placing the diodes very close to the plasma itself.

The CVD detectors used so far on fusion experiments were of the Multilayer Planar configuration shown in Figure 9 (a) but, in order to improve sensitivity to higher energy photons, a new geometry was tested (Cesaroni et al., 2022). In the LAT(eral) configuration (Figure 1 (b)), the crystal is oriented perpendicular to the incident radiation, so that the full length of the crystal, about 3 mm, is available for radiation absorption. A combination of these two types of detectors can provide an optimal detection coverage of the plasma emission in terms of both geometry and energy. A third type, the Interdigitated Electrode configuration, is especially suited to study fast events (Mezi, 2022) and is being considered for the specific monitoring of ELM's, MHD instabilities, pellet ablations, etc.

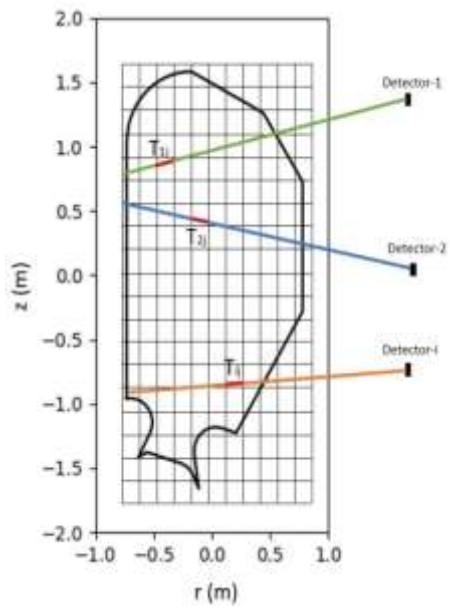


**Figure 10 The pixel grid layout used for tomographic reconstruction of the DTT tokamak, with a matrix element Tij highlighted to represent the weight of the i-th line of sight in the j-th pixel.**

## 3. TOMOGRAPHIC RECONSTRUCTION TECHNIQUES

A pixel-based approach was chosen to evaluate the optimal design for reconstructing X-ray and UV radiation in the DTT tokamak. The region to be reconstructed was divided into a grid of $n_{pixel} = n_x \times n_y$ small rectangular pixels to achieve a constant emissivity, $g$, in each of them. The integral equation of the brightness was discretized through the relation:

$$f_i = \sum_{j=1}^{n_{pixel}} T_{ij} g_j$$

Here, $T_{ij}$ is a $n_{LoS} \times n_{pixel}$ matrix that contains the weight of the LoS in each pixel, which is determined by the length of the i-th line-of-sight (LoS) in the j-th pixel, as shown in Figure 10. The fundamental indeterminacy of tomographic reconstruction can result in the problem being solved in an

infinite number of ways, and *a priori* conditions are generally introduced to minimize errors in the reconstruction process. One option uses the minimization of $\chi^2$ with the Tikhonov regularization matrix $\mathbf{H} = \mathbf{\Gamma}^T \cdot \mathbf{\Gamma}$ [Anton et al., 1996]. The minimization equation is:

$$\varphi = \chi 2 + \lambda\, g^{\,T}\, \mathbf{H}\, \mathbf{g}\, \mathbf{T}^T,$$

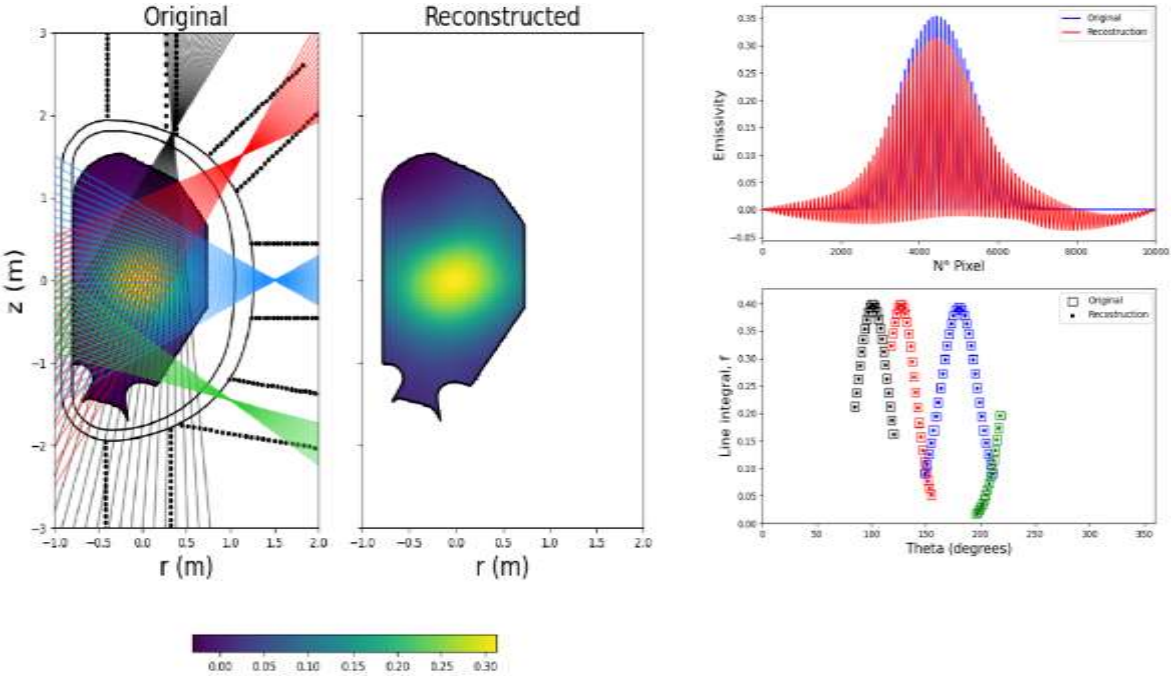


**Figure 11 Comparison of the original and reconstructed data for the Gaussian phantom, line integral along the LoS, and emissivity as a function of pixels using a matrix of 100 x 100 pixel and 96 LoS.**

and the reconstructed emissivity is given by: $\boldsymbol{g}_{meas} = (\boldsymbol{T}^{\,T} \cdot \mathbf{T} + \lambda \mathbf{H})^{-1} \cdot \mathbf{T}^{\,T} \cdot \boldsymbol{f}_{meas}$. The reconstructed emissivity is the parameter that determines whether the regularization used is correct and, therefore, whether the reconstruction algorithm works effectively.

## 4. TOMOGRAPHY DIAGNOSTIC LAY-OUT

The tomography system will be installed in one sector of the DTT tokamak, provided with 4 ports (a fifth one, at the bottom, is essentially blind); the space has to be shared with other diagnostics, in particular the bolometry system, and other auxiliary systems such as cooling pipes, therefore the most compact design is highly desirable. In order to optimize the detectors spatial distribution and their number, a Python software was developed to determine the quality of the reconstructed images for different detector configurations. The goal was to reconstruct, by means of the inversion techniques described in the previous section, a two-dimensional Gaussian function centered at the origin defined by the equation:

$$f(x,y) = \frac{1}{2\pi\sigma^2} e^{-\frac{x^2+y^2}{2\sigma^2}}$$

In this study, the width of the emission profile σ was set to 0.45, to simulate the broad emission to be expected in DTT. For this phantom type, the regularization matrix used is the gradient matrix. Initial tests were conducted to determine the best compromise between computational speed and image resolution, with 96 detectors and reasonable viewing angles (see Table I). The best results were obtained using an array of 100 x 100 pixel. Further tests were carried out to determine the minimum number

**Table I. Distribution of detectors in each port for the initial configuration of Figure 3 and that of Figure 4**

| Port # | # LoS | Opening Angle (°) | # LoS | Opening Angle (°) |
|---|---|---|---|---|
| **1** | 24 | 35 | 24 | 35 |
| **2** | 24 | 37 | 12 | 30 |
| | | | 12 | 38 |
| **3** | 32 | 62 | 16 | 55 |
| | | | 16 | 45 |
| **4** | 16 | 22 | 16 | 55 |
| | **Figure 3** | | **Figure 4** | |

of lines required for a good reconstruction while using the least possible number of devices. It was found that a reconstruction made with more than 100 LoS does not yield significant improvements, while lower number of LoS steadily degrade the quality of the reconstructed image, thus confirming the validity of the initial choice. The reconstruction shown in Figure 9Figure 11 is very similar to the original one, but increasing the number of nodes can further improve both spatial coverage and accuracy of the emissivity reconstruction in the peripheral regions. Figure 4 shows a reconstruction of the Gaussian phantom performed with 96 lines of sight, doubling the number of nodes in ports 2 and 3 and

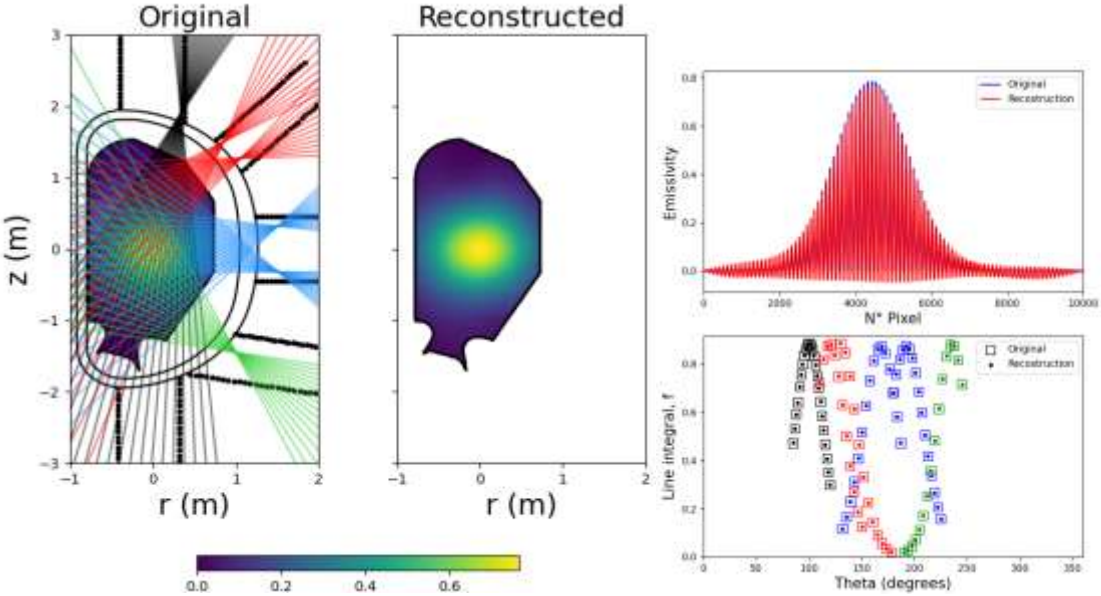


**Figure 12 Same as Figure 3 but with two nodes in Ports 2 and 3, and a wider viewing angle in Port 4**

increasing the opening angle of the node in port 4 (this can be problematic in practice). Additional tests, including more complex phantoms, are underway.

## 5. CONCLUSIONS

The preliminary design of a Tomography diagnostic system for DTT is based on the use of thin, single crystal CVD diamond detectors. While conventional Si or CdTe diodes are not ruled out, their placement in the harsh environment of the machine would be challenging.

The detectors distribution is being driven by the results of tomographic reconstructions of simulated plasma emission profiles by means of a pixel-based code *ad hoc* developed that uses the minimization of $\chi^2$ with the Tikhonov regularization. The number of pixels affects mostly the computational time, but a 100 x 100 matrix is adequate for a good reconstruction, with about 100 detectors. The other most important factors influencing the quality of the reconstruction have turned out to be the number of nodes and the aperture angles of the lines of sight.

## 6. REFERENCES

Ambrosino, R., et al., (2021) *Fus. Eng. & Des.* **167**: 112330
Angelone, M., et al., (2010) *Nucl. Instrum. Methods* A **623**: 726
Anton, M., et al, (1996) *Pl. Phys. Control. Fus* **38.11**: 1849
Bombarda, F., et al., (2021) *Nucl. Fusion* **61**: 116004
Cesaroni, S., et al., (2022), 32nd SOFT, Dubrovnik (Croatia), Poster P-1.297
Mezi, L., et al., (2022) *Il Nuovo Cimento* **45 C** 88
Pillon, M., et al., (2008) *J. Appl. Phys.* **104**: 054513

**Return**

# CCD DIRECT DETECTION ON A SPRED SPECTROMETER

U.A. Sheikh[1] and B.P. Duval[1]

[1]EPFL, Swiss Plasma Center (SPC), CH-1015 Lausanne, Switzerland
Email: umar.sheikh@epfl.ch

**Abstract**

This paper presents the installation and performance of a direct UV photon charge-coupled device (CCD) device on the SPRED spectroscopy system of the TCV tokamak. The legacy SPRED detector, based on a micro-channel plate (MCP) UV conversion design, had limitations related to sensitivity to electromagnetic fields, as well as susceptibility to damage from arcing. To address these issues, a solid-state, thinned back-illuminated CCD detector was selected. A novel alignment methodology, with He-Ne 632.8nm lasers, precisely aligned the gratings resulting in unrotated dispersed spectral images. The CCD detector demonstrated improved performance over the legacy system with a reduced full width half maximum (FWHM) and reliable operation for over 20,000 pulses, providing valuable insights into plasma composition and assisting long-term machine conditioning studies.

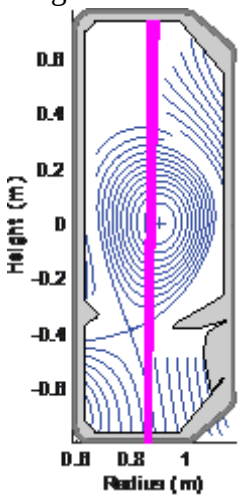


Figure 13 - SPRED line of sight on the TCV tokamak (magenta). Standard plasma configuration overlaid (blue).

## 13. INTRODUCTION

Spectroscopic measurements are crucial for tokamak research as they provide valuable information on plasma composition, power loss channels and plasma-wall interactions. Coupled with modelling tools, these measurements can also be used to infer ion transport rates, elemental ionisation balance and spatial distributions. In particular, the vacuum ultraviolet (VUV) spectral range measures plasma emission in the 10-130 eV range from incompletely ionised elements in the core and divertor. These are typically made using a "survey, poor resolution, extended domain" (SPRED) spectrometer. The TCV tokamak employs such a SPRED system with a vertical line of sight that integrates emission from the core and divertor, as shown in Figure 1.

## 14. SPRED SPECTROMETER AND DETECTOR

TCV's SPRED system is a McPherson 251 grazing incidence spectrometer with a focal length of 0.2 m and an F-number of 14. Its grating mount supports two externally selectable gratings: 450 g/mm and 2105 g/mm. The system is designed to operate under ultra-high vacuum system with a windowless view of the TCV plasma to remove absorption of VUV photons.

### 14.2 Legacy detector design

The legacy SPRED detector employed a photocathode on a micro-channel plate (MCP) to convert photons to primary electrons. A high voltage across MCP amplifies this signal, as an image, with a near exponential gain response. The exiting electrons impinge upon a green phosphor deposited on a coherent fibreoptic bundle. The fibreoptic array had a tapered design to reduce the final width of the spectra, allowing for a larger spectral range to be recorded by the Reticon array. These components of the detector are presented in Figure 2.

The shortcomings of this design were primarily related to the MCP. Specifically, the MCP is sensitive to electromagnetic fields from the tokamak, which can be exacerbated by a plasma disruption that can result in data loss or require a detector reset. Additionally, increases in neutral pressure within the TCV vessel from impurity seeding working gas plasma fuelling often led to a pressure rise at the MCP followed by arcing and consequent damage, altering system sensitivity over time. Furthermore, the alignment and calibration that could be achieved was limited as this

system could only be aligned under vacuum and only integrated the image in the vertical direction (1D detector with 2.5mm high pixels).

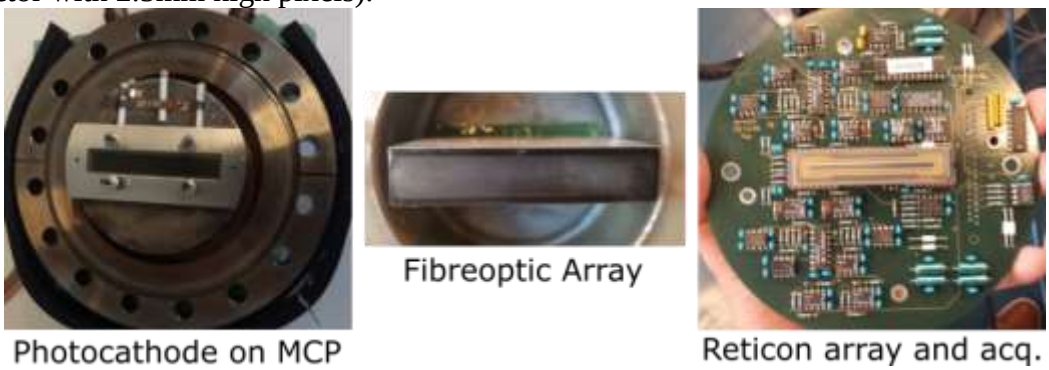


Figure 14 - Legacy SPRED detector design with front end (left), tapered fibreoptic array (middle) and Reticon array with acquisition (right)

### 14.3 New Detector Selection

To overcome the limitations of the MCP in the hostile tokamak environment and increase system reliability, a direct photon detection approach, via a thinned back-illuminated solid-state sensor, was selected. The electrodes on a front-illuminated charge-coupled device (CCD) would stop VUV photons. In the last decade, back-illuminated chips with a thinned silicon substrate have become more common, making them accessible for low-light level and short-wavelength applications. The detector selected was a Greateyes™ full-frame back-illuminated CCD, consisting of 2048 x 512 pixels of size 13.5 µm x 13.5 µm. A full-frame CCD was preferred as 2D images allow for precise alignment and calibration. The downside of this design has low temporal resolution (~10x ms) due to slow readout speeds.

The CCD is mounted onto a vacuum flange in the standard camera design and this was not compatible with the detector mounting assembly on the spectrometer. The sensor chip was mounted with an offset on the flange so that it was in the spectrometer's focal plane, Figure 3. A Peltier cooler on a cooling copper block was used to ensure CCD cooling in vacuum. An electromagnetic shield was installed to reduce pickup on the exposed cables. A slit in the front of the shield reduced the effective active CCD area, to reduce stray radiation in the spectrometer reaching the detector.

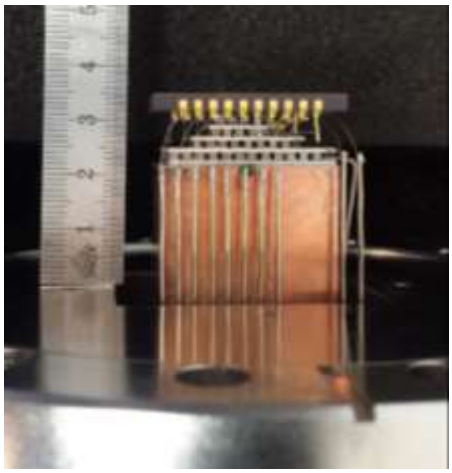

Figure 15 - Offset sensor with Peltier cooler and copper heatsink

## 15. NOVEL ALIGNMENT METHODOLOGY AND CALIBRATION

The system is operated under high vacuum to allow VUV transmission, requiring repeated pumping and venting during alignment, together with cycling the calibration source. A novel methodology was developed with visible light from 632.8nm HeNe lasers. To increase the precision of the process, the laser was aligned over long paths with apertures placed in the beam path. Coarse adjustment of the grating position and angle (α) was achieved by placing one laser at the grating normal and another at the entrance slit. The intersection of the two is the required grating position. The incident angle could then be set by ensuring that the laser normal to the grating was reflected directly back to its source and the 0th and 2nd order reflections of the laser incident on the slit reached calculated locations, marked on the ports, Figure 4a. This approach gave an accuracy in α of 0.5° and 2.3° for the 450g/mm and 2105g/mm gratings respectively. Final fine alignment was performed using the 0th order (reflection) of a fluorescent lamp captured by offsetting the CCD on the detector flange. A laser was not used here to prevent damage to the CCD. The two-dimensional imaging of the detector allowed for any image rotation due to grating tilt to be taken out of the

system, as shown in Figure 4b. The final accuracy in α achieved was estimated at 0.1° for both gratings.

Final VUV alignment and calibration was conducted with a hollow cathode lamp directly coupled to the SPRED using differential pumping (Danzmann 1988). The lamp was placed on a mount with a vacuum bellows allowing it to be scanned across the entire etendue of the spectrometer. The adjustable detector assembly was then used to focus across the whole detector with example images shown in Figure 5. The final full width half maximum (FWHM) of the 30.4nm spectral line was less than half of that from the legacy detector and comparable to the original design paper albeit using an entrance slit width twice as large (Fonck 1982). Table 1 gives an overview of these values with a comparison to one of the original systems installed on JET.

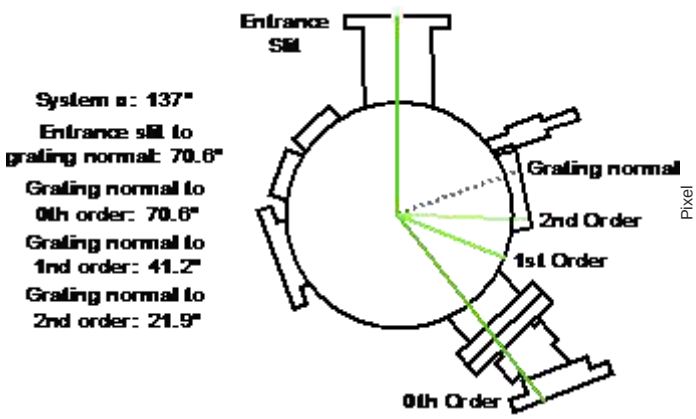


Figure 17a - Schematic of laser alignment

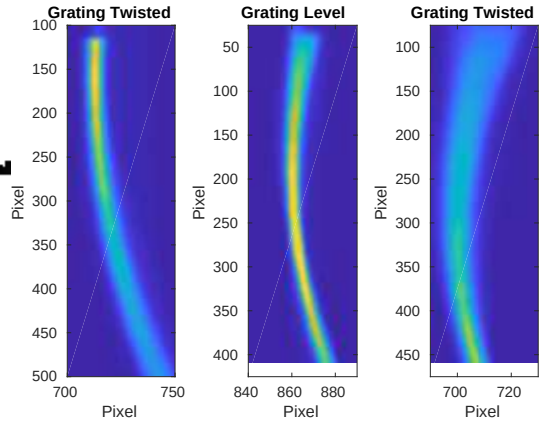


Figure 17b - Images with twisted and level grating

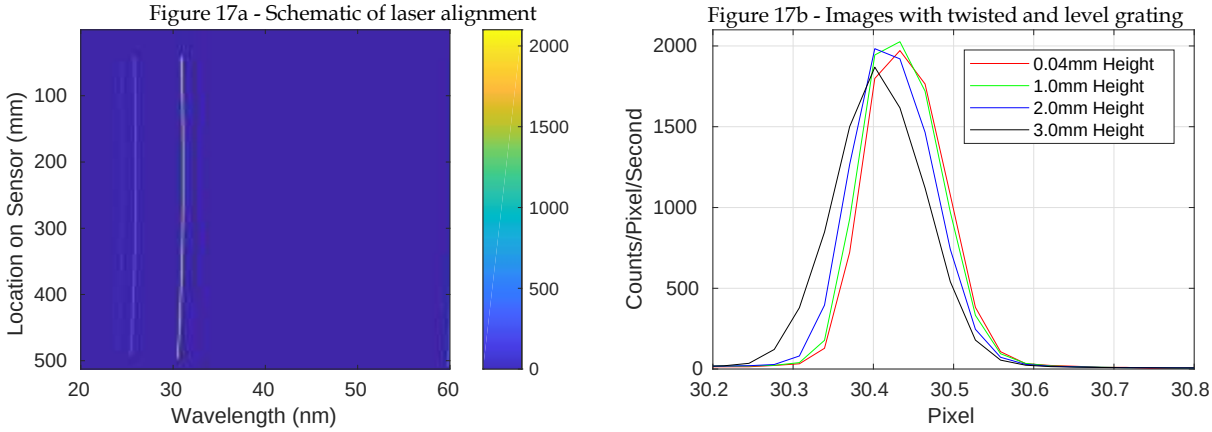


Figure 18 - Image produce using the hollow cathode lamp (left). Spectral line produced as a function of binning height on the sensor (right)

**Table 1. Comparison of FWHM achieved on JET, the SPRED design paper, TCV legacy detector and the CCD detector established in this work**

| System | Slit Width (µm) | Image Height (mm) | FWHM (A) | Slit Width | Image Height (mm) | FWHM (A) |
|---|---|---|---|---|---|---|
| | 450 g/mm | | | 2105 g/mm | | |
| JET | N/A | N/A | 5 | N/A | N/A | 1.5 |
| Fonck 1988 | 25 | 1 | 2 | N/A | N/A | N/A |
| TCV legacy | 50 | 4 | 5 | 50 | 4 | 2 |
| TCV CCD | 50 | 2 | 2.5 | 50 | 2 | 0.7 |

Operating the hollow cathode lamp with prescribed parameters enabled a sensitivity calibration of the detector at the wavelengths of known emission lines (Danzmann 1988). The inverse sensitivity of the two gratings is presented in Figure 7. The values from the JET system that uses an MCP detector, are superimposed for comparison (Lawson 2009). Both gratings show a decrease in inverse sensitivity at longer wavelengths, where the reflectivity of the grating increases. Surprisingly, the inverse sensitivity between 20-40nm is similar for the JET system with an MCP

and the TCV system with a CCD. Conversely, the JET system shows an increase in inverse system sensitivity with increasing wavelength, attributed to the differences in the detector responses. It should be noted that the JET system sensitivity changes with MCP gain and the values reported here are taken for a fixed gain (Lawson 2009).

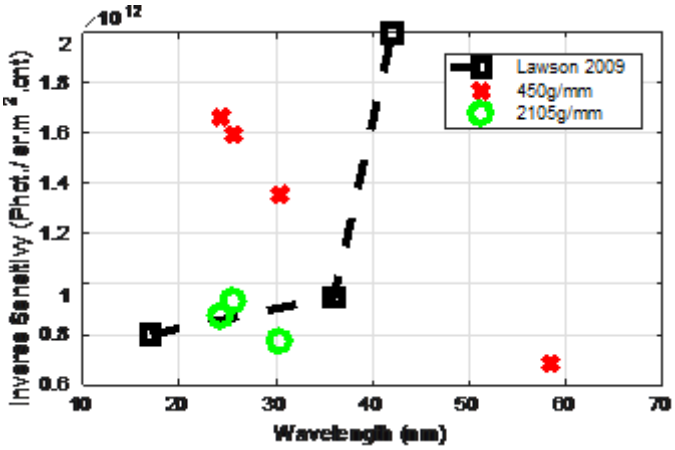


Figure 19 - System sensitivity and comparison with the JET SPRED system

## 16. RESULTS FROM TCV TOKAMAK

Measurements made during plasma operation yielded high resolution spectra with the full etendue of the spectrometer. Sample spectra are shown in Figure 8 for a standard Ohmic discharge (red), nitrogen seeded discharge (green) and with neutral beam injection that resulted in metal impurities being sputtered into the plasma (blue). The detector position was adapted for the beam injection discharge to capture spectral lines at shorter wavelengths. The large apparent FWHM at these shorter wavelengths is not due to system performance but to a high density of numerous metal impurity lines between 10-20nm.

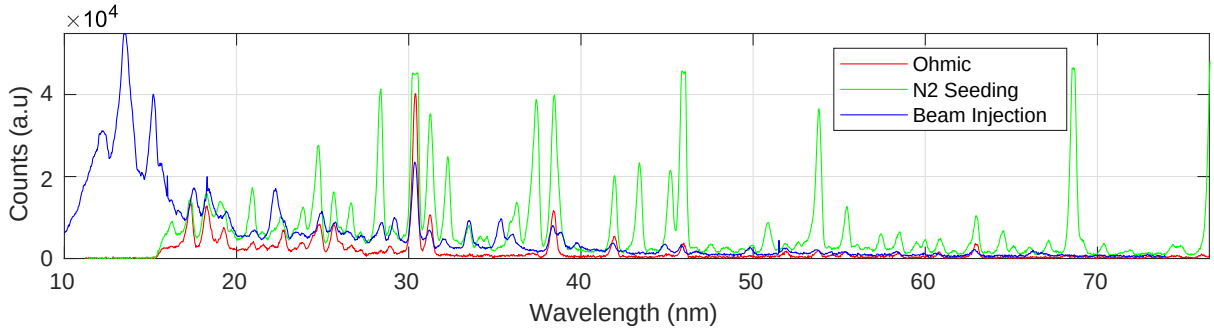


Figure 20 - Sample spectra for a standard Ohmic discharge (red), nitrogen seeded discharge (green) and metal impurities injected into the plasma through sputtering of the neutral beam injection duct (blue).

The system has been now operating reliably for over 20,000 pulses since March 2017. The only system failure during this period was of the Peltier cooler that prevented on chip binning due to thermal leakage, leading to a reduction in temporal resolution to around 100ms. The reliability of the system has permitted long-term analyses of machine conditioning and impurity evolution in the plasma. An example of this is presented in Figure 9, where four spectral ranges were integrated at plasma breakdown for ~110 discharges. The first 20 discharges are in standard operation and low plasma emission is measured at wavelengths between 16-40nm. Between discharges #67832 and #67897, negative triangularity configurations were performed resulting in plasma contact with virgin surfaces on the low field (outer) side of the tokamak. During this period, the spectral emission between 16-40nm was significantly increased, indicating higher impurity content in the plasma. The increased impurity content is attributed to

higher outgassing and sputtering of the virgin surfaces interacting with the plasma. Furthermore, a number of discharges have no spectral data due to failed breakdowns, again resulting from increased impurity content.

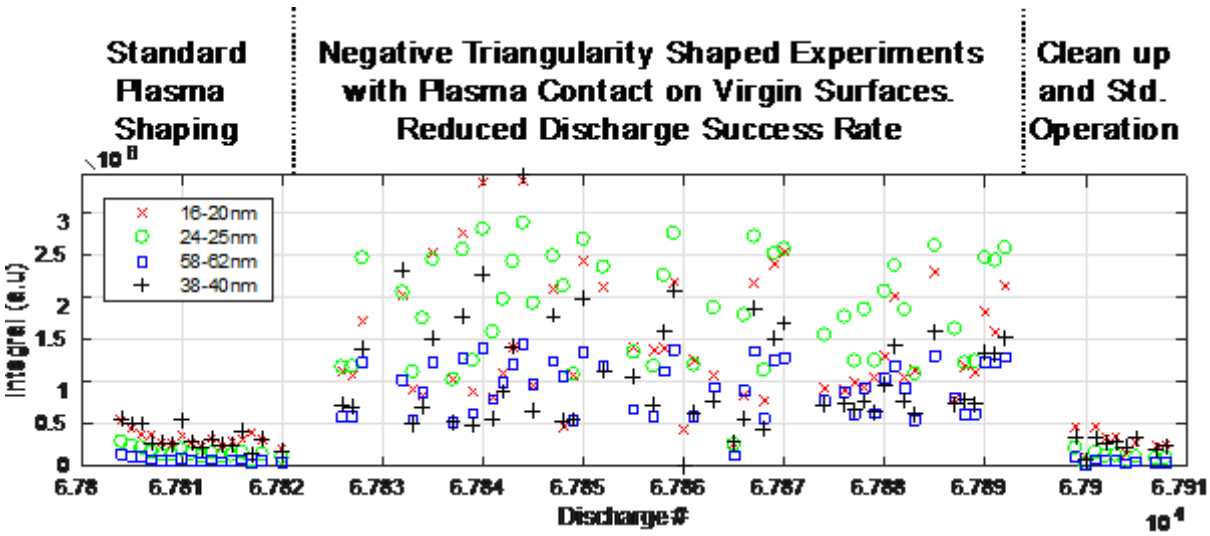


Figure 21 – Integrals of spectral regions at plasma breakdown during standard operation and negative triangularity shaped plasmas.

## 17. CONCLUSIONS

A direct detection CCD detector was installed on the SPRED spectrometer on TCV. A novel alignment method was applied to align the gratings to an α of ~0.1° and reduce image rotation. The FWHM achieved through this process was less than half that of the original detector. The sensitivity of the system was found to be comparable to the JET system with an MCP detector. The system has now performed reliably on TCV for over 20,000 pulses, providing information on plasma composition and aiding in long term machine conditioning studies. These results demonstrate the advantages of a CCD detector for SPRED systems on tokamaks.

## 18. ACKNOWLEDGMENTS

This work was supported in part by the Swiss National Science Foundation.

## 19. REFERENCES

Danzmann, K., et al., “High current hollow cathode as a radiometric transfer standard source for the extreme vacuum ultraviolet,” Appl. Opt. 27, 4947–4951 (1988).

Fonck, R. J., A. T. Ramsey, and R. V. Yelle. "Multichannel grazing-incidence spectrometer for plasma impurity diagnosis: SPRED." Applied Optics 21.12 (1982): 2115-2123

Lawson, K. D., et al. "An absolute sensitivity calibration of the JET VUV SPRED spectrometer." Journal of Instrumentation 4.04 (2009): P04013.

**Return**

# Status of the Development and Testing of In-Vessel and ECH-Protection Components for the ITER Low-Field Side Reflectometer

C.M. Muscatello[1], J.P. Anderson[1], R.L. Boivin[1], F. Cometa[1], R. Fair[2], D.K. Finkenthal[3], A. Forsman[1], D. Fox[1], R. Gar[1], A. Gattuso[1], G.J. Kramer[2], M. LeSher[1], F. Martinez[1], S. Shirey[1], A. Sirinelli[4], D. Su[1], K. Thackston[1], A. Zolfaghari[2]

[1]General Atomics, San Diego, California, USA
[2]Princeton Plasma Physics Laboratory, Princeton, New Jersey, USA
[3]Palomar Scientific Instruments, San Marcos, California, USA
[4]ITER Organization, St Paul Lez Durance, France
E-mail of corresponding author: muscatello@fusion.gat.com

## 20. INTRODUCTION

The ITER Low-Field Side Reflectometer (LFSR) will provide critical information about the edge electron density, fluctuations, and plasma rotation. The plasma-facing antennas will be located in an equatorial port at the outboard midplane of the ITER tokamak. An end-to-end description and a system-wide performance assessment of LFSR have been given previously[1,2]. In addition, a performance assessment focused on in-vessel microwave components has been reported[3]. In this paper, new work and the current status of various microwave components of the in-vessel and ECH-protection sub-systems are discussed. Figure 22 is a CAD model of the vacuum portion of the LFSR transmission line. The components discussed in this paper are:

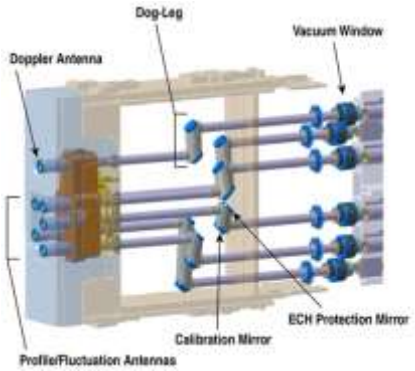


**Figure 22. Front-end portion of the six LFSR transmission lines.**

1. Antenna array: The array consists of 6 monostatic antennas for simultaneous profile, fluctuation, and Doppler measurements. The Doppler antenna is located at the top of the array, well above the midplane. The five lower antennas are for profile and fluctuation measurements and are positioned to accommodate for vertical displacement of the plasma. Performance of the reflectometer depends strongly on the antenna characteristics. Antenna performance, based on modeling and laboratory measurements, is presented in Section 2.

2. ECH protection mirror and monitor: Stray electron cyclotron heating (ECH) power at 170 GHz is a potential threat to the sensitive microwave electronics of the LFSR transceivers. The stray-ECH protection system for LFSR consists of both passive and active components. Passive diffraction gratings are the system's first line of defense. Another layer of defense is a waveguide-integrated power monitor that shutters the diagnostic in the case of a significant stray-ECH event. Modeling and laboratory measurements of a diffraction grating and a conceptual design for the stray-power monitor are presented in Section 3.

3. Vacuum windows: Each transmission line includes a pair of dielectric windows as the vacuum boundary. Windows are a challenge for reflectometer systems because they cause strong spurious reflections, which can lead to measurable reduction to S/N. An anti-reflective solution compatible with ITER requirements has been developed and is discussed in Section 4.

## 21. ANTENNA ARRAY

The majority of the LFSR transmission line consists of 63.5-mm circular, corrugated waveguide which provides broadband, low-loss transmission of the signals[4]. The six antennas are formed from the open end of corrugated waveguide, which is a high-efficiency, high-gain solution for linearly-polarized launch and receive. The five lower antennas are designed for profile and fluctuation measurements and are oriented in horizontal planes for normal launch to the cutoff surface. They are positioned at four unique elevations to accommodate vertical displacement of

the plasma. A Doppler antenna is located at the top of the array and also oriented in a horizontal plane with no poloidal tilt. Because of its elevation it launches obliquely to the cutoff surface, and it has a small toroidal tilt so that it also launches perpendicular to the magnetic field.

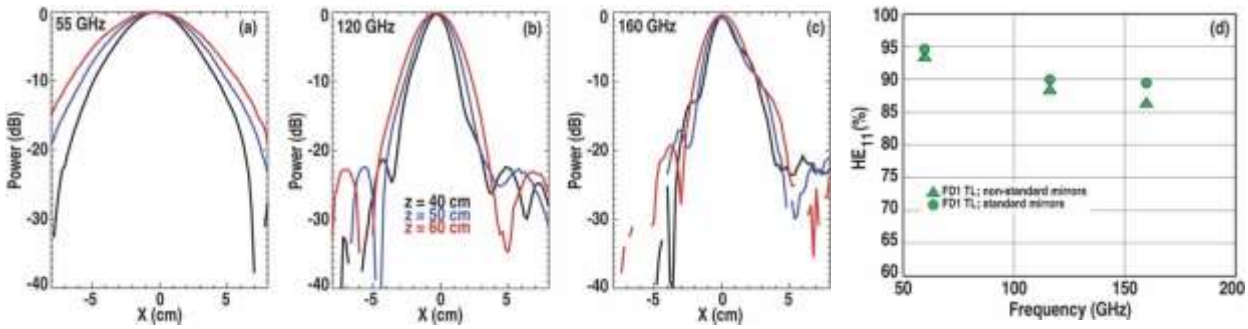


**Figure 24. Antenna patterns at 40, 50, and 60 cm from the antenna for (a)55 GHz, (b)120 GHz, and (c)160 GHz. (d) Power fraction in the $HE_{11}$ mode at the waveguide output.**

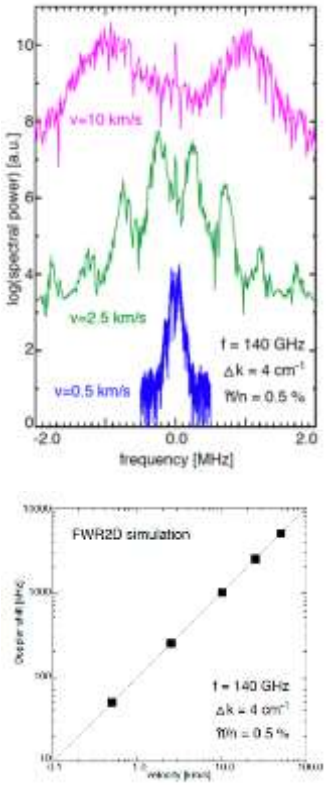


**Figure 23. (a) Spectra from FWR2D for rotation velocities of 0.5 km/s, 2.5 km/s, 10 km/s. (b) Doppler shift of m=1 component vs. velocity.**

As shown in Figure 22, two non-standard mirrors are located in the first two miter bends after each antenna: ECH-protection mirror (diffraction grating) and phase-calibration mirror. The Doppler transmission line lacks the phase-calibration mirror. Antenna pattern measurements at the LFSR test stand were conducted to assess the mode conversion by these non-standard mirrors installed adjacent to the antenna. Measurements with two configurations of the dog-leg mirrors were compared: 1) baseline with standard, flat mirrors and 2) diffraction grating and phase calibration mirror. Antenna patterns for 55 GHz, 120 GHz and 160 GHz are shown in Figure 24(a-c) for Configuration 2 at three different distances from the antenna. The patterns are qualitatively similar for both cases, and low sideband power levels are observed, at or below -20 dB. The effect of the diffraction grating and calibration mirror on the waveguide mode content is quantified with a phase retrieval algorithm using the intensity data collected at each plane from the antenna. The phase retrieval algorithm used here is a combination of an iterative technique[5] and a numerical approach for analyzing beam propagation characteristics[6]. The diffraction grating and calibration mirror cause a small amount of mode conversion compared to standard mirrors. The amount of additional mode conversion increases with frequency, but only up to about 3% smaller $HE_{11}$ power fraction at 160 GHz.

The position and physical orientation of the Doppler antenna were designed to optimize its sensitivity to $k_\perp$ and to maximize the coupled back-scatter, all while staying within the space constraints of the port. The antenna is positioned in a horizontal plane about 1 m above the midplane of the vessel, which is about 50 cm above the nominal midplane of the plasma. To compensate for the ~18° pitch angle of the magnetic field, the antenna is rotated toroidally by 1.5°. With this toroidal rotation, the launch beam is almost perpendicular to the magnetic field. With this orientation, the Doppler system is sensitive to $k_\perp$ = 8 cm$^{-1}$ at 150 GHz, and $k_\perp$ = 4 cm$^{-1}$ at 75 GHz. The FWR2D code was used to verify that these wavenumbers are sufficient for meeting the measurement requirements. Profiles of a full-field (15 MA/5.4 T) ITER H-mode plasma were used. Broadband density fluctuations were generated uniformly over the plasma volume with a radial/poloidal wavenumber distribution centered at $k_r = k_\theta$= 0 cm$^{-1}$ and a spread of $\Delta k_r = \Delta k_\theta$= 4 cm$^{-1}$. The perpendicular group velocity was scanned over a range of 0.5 – 50 km/s (comparable to the measurement requirement of 1 – 50 km/s). With 140 GHz X-mode launch, fluctuation spectra with velocities of 0.5 km/s, 2.5 km/s, and 10 km/s are shown in Figure 23(a). The spectral reflection at DC (zero Doppler shift) is seen in each spectrum, and the Doppler peaks are well resolved even for the lowest simulated velocity. The Doppler shift for the |m| = 1 diffraction order for the 0.5 km/s case is 50 kHz. For the minimum measurement requirement of 1 km/s, the Doppler shift is ~ 100 kHz. The frequencies of the |m| = 1 peaks

are plotted as a function of rotation velocity as shown in Figure 23(b), and the relationship is linear as expected. As for the upper bound of the measurement requirement, a perpendicular velocity of 50 km/s produces a Doppler shift of ~ 5 MHz, which is well within standard analog-to-digital converter (ADC) bandwidth.

## 22. ECH PROTECTION

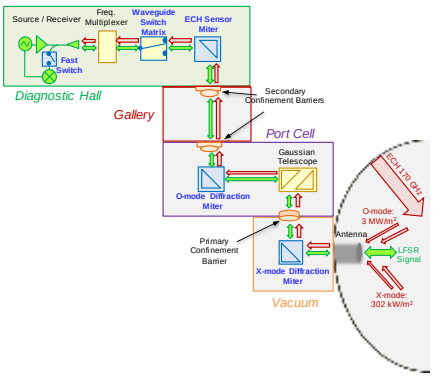


**Figure 25. Basic system-wide schematic of LFSR. The components involved in the ECH protection system are shown in**

High-power electron cyclotron heating (ECH) operating at 170 GHz is a potential threat to the sensitive back-end microwave electronics of the LFSR system. There are two ECH scenarios of concern to LFSR: 1) Breakdown assist: Up to 10 kW (70 dBm) of O-mode polarized power can couple into the LFSR transmission line for 5 seconds at the start of a discharge, and 2) Plasma heating: Up to 1 kW (60 dBm) of X-mode polarized power can couple into the LFSR transmission line for as much as several hundred seconds. Due to the potential for high-power levels of stray ECH reaching the LFSR transceivers, a robust protection system is needed. The LFSR protection system consists of both passive and active components, which are the blue elements of the schematic in Figure 25. The passive protection components provide the first line of defense and these consist of 170-GHz diffraction gratings integrated into miter bends; they are located in the vacuum and port cell regions. The active protection components shutter the back-end electronics in the event of sufficiently high power and these consist of a stray-ECH sensor, corrugated-waveguide switch, and fast switch; they are all located in the diagnostic hall.

Two diffraction gratings are installed within each transmission line. Combined, the two orthogonally-oriented gratings protect against both X- and O-mode stray ECH. The insertion loss ($S_{21}$) of the diffraction grating was quantified at the LFSR test facility, and the measurement result is shown in Figure 26. Up to 160 GHz, there is negligible loss (much less than 1 dB), and the grating acts like a standard mirror. At LFSR's highest operating frequency of 165 GHz, there is an increase in loss (about 5 dB). At 170 GHz there is strong rejection, indicated by the sharp drop in transmission at about -20 dB. Based on these results, the diffraction grating is an effective passive protection mechanism against 170-GHz ECH.

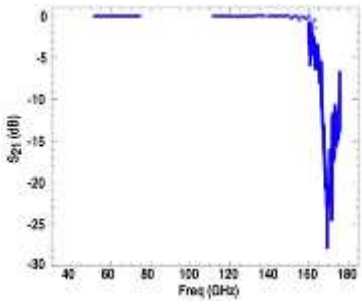


**Figure 26. Insertion loss of 170-GHz diffraction grating.**

Even with 20 dB of protection from the diffraction gratings, up to 100 W (50 dBm) can transmit to the diagnostic hall where the sensitive microwave electronics are located. These components have a damage threshold of about 10 dBm, so a fast-response, active protection system is also incorporated. A stray-ECH sensor will be installed in miter bends just before the waveguide switches (see Figure 25). It must detect mW power levels and activate the fast switch and waveguide switch when the power is over threshold. A key feature of the ECH sensor is a leaky mirror that passes a small fraction of 170 GHz for all incident polarizations. The mirror must not significantly impact the LFSR signal over the frequency range of 30 – 165 GHz. A similar power-monitoring approach for high-power transmission[8] is being pursued for LFSR. A CAD rendering is shown in Figure 27. The mirror consists of two rows of circular holes to couple a small fraction of 170-GHz power into waveguides that direct the power to commercial amplitude detectors. COMSOL results of this leaky-mirror design indicate the power coupling is sufficient to detect the expected range of incident stray-ECH power. Furthermore, the simulation results indicate the design is compatible with arbitrary polarization. Prototype fabrication and test verifications are currently ongoing.

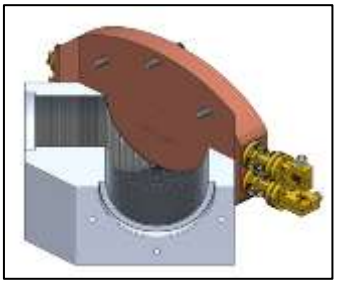

**Figure 27. Miter-bend integrated stray-ECH sensor.**

## 23. VACUUM WINDOWS

Windows are a challenge for reflectometer systems because they generally cause strong spurious reflections. These unwanted reflections can lead to measurable reduction in S/N and clutter in the FMCW signals. In ITER, two windows are required at the vacuum boundary for redundancy. In addition, two secondary confinement barriers are required as a safety measure to prevent tritium ingress in an accident event. This unprecedented number of windows required for the transmission line is a result of the safety standards for such nuclear facilities. Fusion power plants will impose even stricter requirements, necessitating innovative diagnostic solutions for signal transmission.

Anti-reflective (AR) coatings are a very effective way to reduce reflections and interference. Multi-layered dielectric coatings can provide very broadband improvement[9], but these coatings are not generally vacuum compatible and would not withstand the nuclear and thermal loads in ITER. An alternative approach is being considered for the LFSR windows involving metasurfaces. An important feature of this design is that the metasurface is fabricated onto the surface of two quartz wafers that are bonded to both sides of the quartz substrate. The substrate forms the structural component of the window, and the adhesive material used for bonding meets ITER requirements. Optimization modelling of the surface structure was performed with COMSOL. Preliminary measurements are available for a partial window assembly, which consists of an AR wafer bonded to one side of the substrate. Results are shown in Figure 28 for the partial AR assembly. Agreement is excellent between the measured and simulated return loss ($S_{11}$) for both the uncoated substrate and partial AR assembly. With a complete window assembly (both sides coated), modeling predicts an additional 5-dB reduction of $S_{11}$ at 110 GHz, as well as a significant improvement over the full frequency range. Manufacturing development is ongoing, and measurement results with the complete assembly are forthcoming.

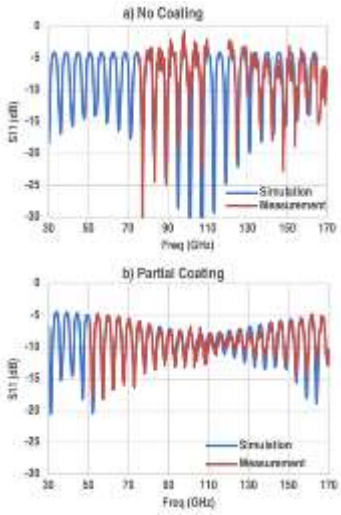


**Figure 28. Return loss ($S_{11}$) for (a) quartz substrate without AR coating and (b) with partial coating.**

## 24. REFERENCES

[1] Muscatello C M, et al., Design overview of the low-field side reflectometer for ITER Proceedings of the 14th International Reflectometry Workshop (Lausanne, Switzerland) p O.113, 2019.
[2] Muscatello C M, et al., Nucl. Fusion **60** 066005, 2020.
[3] Muscatello C M, et al., Rev. Sci. Instrum. **92** 33524, 2021.
[4] Doane J L, Fusion Sci. Technol. **53** 159–73, 2008.
[5] Denison D R, IEEE Trans. Plasma Sci. **27** 512–9, 1999.
[6] Anderson J P, et al., IEEE Trans. Microw. Theory Tech. **50** 1526–35, 2002.
[7] Khayrutdinov R R and Lukash V E, J. Comput. Phys. **109** 193–201, 1993.
[8] Doane J, et al., Fusion Eng. Des. **93** 1–8, 2015.
[9] Nadolski A, et al., Millimeter, Submillimeter, and Far-Infrared Detectors and Instrumentation for Astronomy IX vol 10708, ed J Zmuidzinas and J-R Gao (SPIE) pp 719–31, 2018.

## 25. ACKNOWLEDGMENT*

This work is supported by US DOE Contract No. DE-AC02-09CH11466. All US activities are managed by the US ITER Project Office, hosted by Oak Ridge National Laboratory with partner labs Princeton Plasma Physics Laboratory and Savannah River National Laboratory. The project is being accomplished through a collaboration of DOE Laboratories, universities and industry. The views and opinions expressed herein do not necessarily reflect those of the ITER Organization.

* DISCLAIMER: This report was prepared as an account of work sponsored by an agency of the United States Government. Neither the United States Government nor any agency thereof, nor any of their employees, makes any warranty, express or implied, or assumes any legal liability or responsibility for the accuracy, completeness, or usefulness of any information, apparatus, product, or process disclosed, or represents that its use would not infringe privately owned rights. Reference herein to any specific commercial product, process, or service by trade name, trademark, manufacturer, or otherwise, does not necessarily constitute or imply its endorsement, recommendation, or favoring by the United States Government or any agency thereof. The views and opinions of authors expressed herein do not necessarily state or reflect those of the United States Government or any agency thereof.

**Return**